J. Fluid Mech. (2025), *vol.* 1009, A49, doi:10.1017/jfm.2025.243

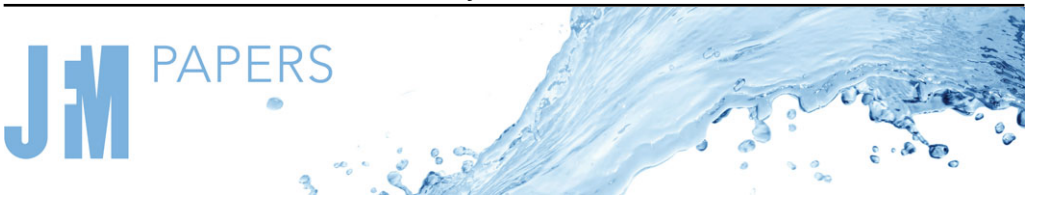

Lattice Boltzmann simulations of Rayleigh–Bénard convection with compressibility-induced non-Oberbeck–Boussinesq effects

Junren Hou[1], **Minyun Liu**[2] **and Shanfang Huang**[1]

[1]Department of Engineering Physics, Tsinghua University, Beijing 100084, PR China

[2]CNNC Key Laboratory on Nuclear Reactor Thermal Hydraulics Technology, Nuclear Power Institute of China, Chengdu 610213, PR China

Corresponding author: Shanfang Huang, sfhuang@mail.tsinghua.edu.cn

(Received 14 November 2024; revised 17 February 2025; accepted 24 February 2025)

To analyse compressibility-induced non-Oberbeck–Boussinesq (NOB-II) effects, we present a lattice Boltzmann (LB) model capable of simulating supercritical fluids. The LB model is validated using analytical solutions and experimental data. Using this model, we conduct two-dimensional laminar LB simulations of Rayleigh–Bénard convection (RBC) in supercritical fluids. Our results reveal that the ratio of the adiabatic temperature difference to the total temperature difference, α, effectively indicates the intensity of NOB-II effects. We find that, NOB-II effects do not break the symmetry of the temperature, density or momentum fields. However, due to density differences between the upper and lower regions, NOB-II effects break the velocity symmetry. Moreover, we report for the first time the density inversion phenomenon in RBC, wherein convection can still occur when the bottom fluid is denser than the top fluid. The condition for density inversion is given as $\alpha > (c_p - c_v)/c_p$, where c_p and c_v are the specific heat capacities at constant pressure and volume, respectively. This inversion is attributed to the coupling effect of a significant pressure gradient and fluid compressibility. Our results also show that for a given Rayleigh number, NOB-II effects have no impact on the Reynolds number. However, as α approaches 1, the Nusselt number decreases linearly towards 1, indicating significant heat transfer deterioration (HTD). The mechanism underlying HTD is attributed to the compression work term in the energy equation, which absorbs heat from the hot plume in central region, diminishing its capacity to transfer heat from the bottom to the top plate.

Key words: Bénard convection, Buoyancy-driven instability, gas dynamics

1. Introduction

Thermal convection plays a critical role in various fields, including meteorology (Tong *et al.* 2017), astrophysics (Pandey *et al.* 2021) and engineering (Huang *et al.* 2024). Rayleigh–Bénard convection (RBC), a system in which a fluid is heated from below and cooled from above, serves as a classical configuration for studying thermal convection behaviour (see Lohse & Shishkina (2024)) and Lohse & Xia (2010)) for reviews). Typically, standard RBC (OB-RBC) is described by the Oberbeck–Boussinesq (OB) approximation, which relies on the following assumptions.

(OB1) Constant properties: the fluid's viscosity μ, thermal conductivity λ, specific heat capacity at constant pressure c_p and isobaric expansion coefficient β are constants.

(OB2) Incompressibility: the fluid is assumed to be incompressible, with buoyancy difference due to density variations being considered.

(OB3) Linear density–temperature relation: the density in the gravity term varies linearly with temperature, following the relationship: $\rho = \rho_m - \rho_m \beta(T - T_m)$. Here, ρ is the density, T is the temperature and ρ_m and T_m are the mean density and temperature, respectively.

However, real fluids are compressible and their properties vary with temperature and pressure. In many natural and industrial systems, substantial temperature and pressure differences cause the OB approximation to break down. This limitation has motivated extensive research into non-Oberbeck–Boussinesq (NOB) effects in RBC (Wan *et al.* 2020).

NOB effects can be categorised into two distinct types (Wan *et al.* 2020). The first type, referred to as NOB-I, involves the temperature-dependent variations in the fluid's physical properties. Under NOB-I conditions, the assumptions OB1 and OB3 no longer hold. Research on NOB-I effects has primarily concentrated on two key parameters: the mean temperature of the centre plane (T_c) and the Nusselt number (Nu) (Yik *et al.* 2020). The mean temperature of the centre plane T_c indicates temperature symmetry, while the Nusselt number Nu reflects heat transfer efficiency. Wu & Libchaber (1991) conducted pioneering experimental studies on RBC in low-temperature helium and were the first to observe symmetry breaking in the temperature field. They discovered that under NOB-I conditions, T_c in helium is greater than T_m. Later, Zhang *et al.* (1997) extended this investigation to glycerol, demonstrating that T_c is also higher than T_m in glycerol. Subsequent experimental and numerical studies have explored NOB-I effects in other common fluids, such as water (Ahlers *et al.* 2006; Sugiyama *et al.* 2009; Demou & Grigoriadis 2019) and air (Wan *et al.* 2020; Pan & Choi 2023, 2024). These studies consistently found that T_c is higher than T_m in both water and air. Moreover, it was observed that Nu slightly decreases in water under NOB-I conditions, while NOB-I effects have a negligible impact on Nu in air.

Due to the drastic changes in the physical properties of supercritical fluids near the critical isochore, many researchers have explored the impact of NOB-I effects in supercritical fluids. Ahlers *et al.* (2008, 2007) experimentally investigated the NOB-I effects of ethane near its critical isochore. They observed that T_c is lower than T_m in the gas-like region, while the opposite is true in the liquid-like region. Additionally, their findings revealed that NOB-I effects lead to an increase in Nu in both regions, indicating heat transfer enhancement. Yik *et al.* (2020) further experimentally studied the NOB-I effects in supercritical SF_6. In their study, they carefully controlled the Rayleigh (Ra) and Prandtl (Pr) numbers to independently regulate the intensity of NOB-I effects. Their results aligned with those of Ahlers *et al.* (2008, 2007), confirming that T_c is lower than T_m in the gas-like region and higher in the liquid-like region. Additionally, they observed heat transfer enhancement up to 112 %. It is important to note that, although supercritical fluids

exhibit high compressibility near the critical isochore, these researchers made significant efforts to minimise the effects of compressibility in their analyses of NOB-I effects.

The second type of NOB (NOB-II) effects focus on the impact of fluid compressibility. Under NOB-II conditions, OB2 and OB3 are no longer satisfied. In compressible fluids, density varies with both temperature and pressure, leading to two unique phenomena: the piston effect and the adiabatic temperature gradient (ATG). The piston effect, an efficient heat transfer mechanism driven by compression waves (Zappoli *et al.* 1990), can induce the oscillations in wall temperature near the onset of RBC, which has attracted significant scholarly attention (Amiroudine *et al.* 2001; Chiwata & Onuki 2001; Kogan & Meyer 2001; Amiroudine & Zappoli 2003; Bouafia & Daube 2021). ATG refers to the additional temperature gradient required to trigger RBC under NOB-II conditions. This concept was first introduced by Giterman & Shteinberg (1970) and has since been supported by numerous theoretical (Carlès & Ugurtas 1999), experimental (Kogan *et al.* 1999; Kogan & Meyer 2001) and numerical (Amiroudine *et al.* 2001; Accary *et al.* 2005; Bouafia & Daube 2021) studies.

Researchers have also focused on the scaling law of $Nu-Ra$ under NOB-II conditions. Ashkenazi & Steinberg (1999) conducted an experimental study on the turbulent convective behaviour of SF_6 near the critical isochore at high Ra (up to 5×10^{14}), while exploring Pr range from 1 to 100. They found that Nu follow the scaling relationship $Nu \propto Ra^{0.3} Pr^{-0.2}$. To further understand how NOB-II effects influence the scaling law of $Nu-Ra$, Kogan & Meyer (2001) experimentally investigated the RBC of ^{3}He near its critical isochore. They introduced a corrected Nusselt number (Nu_{corr}) accounting for ATG. The results show that the convection current based on Nu_{corr} versus the reduced Rayleigh number collapse onto a single curve in steady convective states (Kogan *et al.* 1999; Kogan & Meyer 2001). In the turbulent regime, their findings (Kogan & Meyer 2001) indicated that Nu_{corr} and Ra follow a 2/7 power law, $Nu \propto Ra^{2/7}$, within the range $10^5 < Ra < 10^7$. This conclusion was further supported by Accary *et al.* (2009), who conducted three-dimensional (3-D) numerical simulations of RBC in a supercritical fluid described by the van der Waals equation of state.

Although previous studies have reported the impact of NOB-I effects on the temperature symmetry, it remains unclear whether NOB-II effects lead to similar symmetry breaking. Furthermore, while the scaling law of $Nu-Ra$ under NOB-II conditions has been investigated, a clear understanding of the role of NOB-II effects on heat transfer is still lacking. To address these gaps, advanced numerical methods are required.

Previous numerical methods have used various approximations to simplify the solution of the Navier–Stokes equations, such as acoustic filtering (Accary *et al.* 2009; Shen & Zhang 2012) and anelastic approximation (Bouafia & Daube 2021). These methods are insufficient for fully capturing the intricate details of RBC under NOB-II conditions. For example, Bouafia & Daube (2021) used a stratification density approach to simplify the solution of the density. This model is just 'an extended Boussinesq approximation using a stratified density field', as Bouafia & Daube (2021) stated. The lattice Boltzmann method (LBM), as a mesoscopic method, has great potential for modelling compressible fluids. It has been widely applied in fields such as multiphase flow (Li *et al.* 2015; Huang & Wu 2016; Chen *et al.* 2022; Gong *et al.* 2024), porous media flow (Jiang *et al.* 2021) and turbulent flow (Chen *et al.* 2003). Moreover, this method provides a clear physical representation and can effectively reveal the underlying mechanisms of convective heat transfer. Therefore, LBM is employed in this study to investigate NOB-II effects. Moreover, following the previous research (Kogan *et al.* 1999; Kogan & Meyer 2001; Ahlers *et al.* 2007, 2008; Accary *et al.* 2009; Yik *et al.* 2020; Bouafia & Daube 2021),

a supercritical fluid is selected for study due to its high compressibility near the critical isochore.

In this work, we present a lattice Boltzmann (LB) model capable of simulating supercritical fluids. The model is validated using the static cavity, Schwarzschild criterion and experimental data of Kogan *et al.* (1999). Using this model, we perform LB simulations of RBC in supercritical fluids. Our results reveal that, unlike NOB-I effects, NOB-II effects do not cause symmetry breaking in temperature, density and momentum fields. However, due to density differences between the upper and lower regions, NOB-II effects break the symmetry of the velocity field. Moreover, NOB-II effects lead to the phenomenon of density inversion, wherein convection can still occur when the bottom fluid is denser than the top fluid. To our knowledge, this is the first report of density inversion in RBC. Additionally, we find that for a given Ra, NOB-II effects have no impact on the Re, while Nu decreases linearly to 1 as NOB-II effects strengthen, indicating significant heat transfer deterioration (HTD).

The rest of the paper is organised as follows. In § 2, the details of the LB model are presented. Then, the model is validated in § 3 using the static cavity, Schwarzschild criterion and experimental data. The main results and discussions are presented in § 4. We first investigate the impact of NOB-II effects on the symmetry of the temperature, density and momentum fields. Then, we explore the phenomenon of density inversion and the mechanism behind it. Finally, we analyse the impact of NOB-II effects on heat transfer and reveal the mechanism behind HTD. In § 5, the main findings of this study are summarised and future research directions are discussed.

2. Numerical method

2.1. *Lattice Boltzmann method*

A lattice Boltzmann model consists of the following three parts: the evolution equation for the distribution function, the equilibrium distribution function and the discrete velocity model. Our model is developed based on the LB model proposed by Guo *et al.* (2002), which incorporates the external force term. The evolution equation for the distribution function is given by

$$f_i(\boldsymbol{x}+\boldsymbol{e_i}\delta_t, t+\delta_t) = f_i(\boldsymbol{x}, t) - \frac{1}{\tau}\left(f_i - f_i^{eq}\right) + \delta_t\left(1-\frac{1}{2\tau}\right)F_i, \tag{2.1}$$

where f_i is the distribution function, $\boldsymbol{x}$ is the position vector, t is the time, δ_t is the time step and τ is the relaxation time, which is related to the kinematic viscosity ν:

$$\tau = \frac{\nu}{c_s^2\delta_t} + \frac{1}{2}. \tag{2.2}$$

Here, $c_s = c/\sqrt{3}$ is the sound speed and $c = \delta_x/\delta_t$ is the lattice speed. The equilibrium distribution function f_i^{eq} is given by

$$f_i^{eq} = w_i\rho\left[1 + \frac{\boldsymbol{e_i}\cdot\boldsymbol{u}}{c_s^2} + \frac{(\boldsymbol{e_i}\cdot\boldsymbol{u})^2}{2c_s^4} - \frac{\boldsymbol{u}\cdot\boldsymbol{u}}{2c_s^2}\right], \tag{2.3}$$

where w_i is the weight coefficient, $\boldsymbol{u}$ is the velocity. We employ the D2Q9 discrete velocity model, which comprises nine discrete velocities. The nine discrete velocities are defined

as follows (Qian *et al.* 1992):

$$\boldsymbol{e_i} = \begin{cases} (0,\,0), & i = 0, \\ c\left(\cos\left[(i-1)\frac{\pi}{2}\right], \sin\left[(i-1)\frac{\pi}{2}\right]\right), & i = 1{-}4, \\ \sqrt{2}c\left(\cos\left[(2i-1)\frac{\pi}{4}\right], \sin\left[(2i-1)\frac{\pi}{4}\right]\right), & i = 5{-}8. \end{cases} \tag{2.4}$$

The corresponding weight coefficients are given by

$$w_i = \begin{cases} 4/9, & i = 0, \\ 1/9, & i = 1{-}4, \\ 1/36, & i = 5{-}8. \end{cases} \tag{2.5}$$

The macroscopic velocity $\boldsymbol{u}$ and density ρ are calculated as follows:

$$\rho \boldsymbol{u} = \sum_i f_i \boldsymbol{e_i} + \frac{\delta_t}{2}\boldsymbol{F}, \quad \rho = \sum_i f_i. \tag{2.6a,b}$$

The external force term F_i in (2.1) is given by

$$F_i = w_i \left[\frac{\boldsymbol{e_i} - \boldsymbol{u}}{c_s^2} + \frac{(\boldsymbol{e_i}\cdot\boldsymbol{u})\,\boldsymbol{e_i}}{c_s^4}\right]\cdot\boldsymbol{F}\,. \tag{2.7}$$

To make the LB model able to simulate supercritical fluids, we introduce the intermolecular forces proposed by Shan & Chen (1993, 1994), defined as follows:

$$\boldsymbol{F_m}(\boldsymbol{x}) = -\frac{3}{\delta_t} G\psi(\boldsymbol{x}) \sum_i w_i \psi(\boldsymbol{x} + \boldsymbol{e_i}\delta_t)\boldsymbol{e_i}, \tag{2.8}$$

where G is the interaction strength, which is set to -1. At this point, the total force includes intermolecular forces and gravity:

$$\boldsymbol{F} = \boldsymbol{F_m} + \boldsymbol{F_g} = \boldsymbol{F_m} + \rho\boldsymbol{g}, \tag{2.9}$$

where $\boldsymbol{g}$ is the acceleration due to gravity. The corresponding macroscopic equations can be derived from the Chapman–Enskog expansion (Guo *et al.* 2002).

Continuity equation:

$$\frac{\partial\rho}{\partial t} + \boldsymbol{\nabla}\cdot(\rho\boldsymbol{u}) = 0. \tag{2.10}$$

Momentum equation:

$$\frac{\partial(\rho\boldsymbol{u})}{\partial t} + \boldsymbol{\nabla}\cdot(\rho\boldsymbol{u}\boldsymbol{u}) = -\boldsymbol{\nabla}p + \boldsymbol{\nabla}\cdot\left[\rho\nu(\boldsymbol{\nabla}\boldsymbol{u} + \boldsymbol{\nabla}\boldsymbol{u}^{\mathrm{T}})\right] + \rho\boldsymbol{g}. \tag{2.11}$$

Here, p is the pressure, expressed in the following form (He & Doolen 2002):

$$p = \rho c_s^2 + \frac{Gc^2}{2}\psi^2 + O(\nabla^2\psi). \tag{2.12}$$

Therefore, to ensure that the $p{-}\rho{-}T$ relationship satisfies the given equation of state, the pseudopotential ψ should take the following form:

$$\psi(\boldsymbol{x}) = \sqrt{\frac{2\left(p_{EOS} - \rho c_s^2\right)}{Gc^2}}, \tag{2.13}$$

where p_{EOS} is the pressure given by the equation of state.

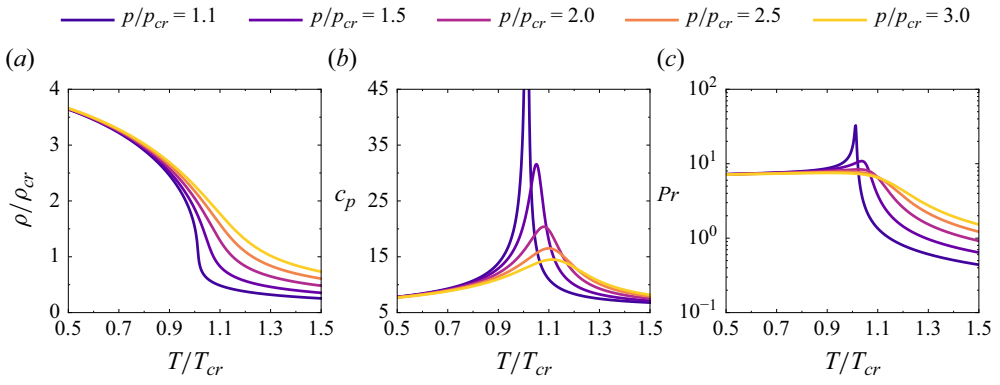

Figure 1. Variation of (*a*) density ρ, (*b*) specific heat at constant pressure c_p and (*c*) Prandtl number Pr with temperature for various pressures.

2.2. *Equation of state*

In this study, we adopt the Peng–Robinson equation of state (Peng & Robinson 1976):

$$p(T, \rho) = \frac{\rho RT}{1 - b\rho} - \frac{a\varphi(T)\rho^2}{1 + 2b\rho - b^2\rho^2}, \tag{2.14}$$

where

$$\varphi(T) = \left[1 + \left(0.37464 + 1.54226\omega - 0.26992\omega^2\right)\left(1 - \sqrt{T/T_{cr}}\right)\right]^2, \tag{2.15}$$

$$a = 0.45724 R^2 T_{cr}^2 / p_{cr}, \tag{2.16}$$

$$b = 0.0778 R T_{cr} / p_{cr}. \tag{2.17}$$

Here, R represents the gas constant, ω is the acentric factor, T denotes the temperature and 'cr' denotes the critical point properties. In this study, we use the values $a = 2/49$, $b = 2/21$, $R = 1$ and $\omega = 0.344$, which are commonly employed to characterise the physical properties of water (Chen *et al.* 2022; Shah *et al.* 2023). From (2.16) and (2.17), the critical point physical properties can be obtained as $T_{cr} = 0.0778a/(0.45724bR) = 0.07292$ and $p_{cr} = 0.0778^2 a/(0.45724b^2) = 0.05957$. Substituting T_{cr} and p_{cr} into (2.14) yields the critical density $\rho_{cr} = 2.5419$. Figure 1(*a*) shows the variation of density with temperature for various pressures. It can be seen that the density is drastically affected by pressure and temperature near its critical isochore.

2.3. *Energy equation*

We adopt finite difference method to solve the energy equation, which can be expressed as follows (Moukalled *et al.* 2016):

$$\frac{\partial T}{\partial t} = -\boldsymbol{u} \cdot \nabla T + \frac{1}{\rho c_v} \nabla \cdot (\lambda \nabla T) - \frac{T}{\rho c_v} \left(\frac{\partial p}{\partial T}\right)_\rho \nabla \cdot \boldsymbol{u}, \tag{2.18}$$

where λ represents the thermal conductivity and c_v is the specific heat at constant volume. The specific heat at constant pressure, c_p, can be calculated using

$$c_p = c_v - \frac{T}{\rho^2} \left(\frac{\partial \rho}{\partial T}\right)_p \left(\frac{\partial p}{\partial T}\right)_\rho. \tag{2.19}$$

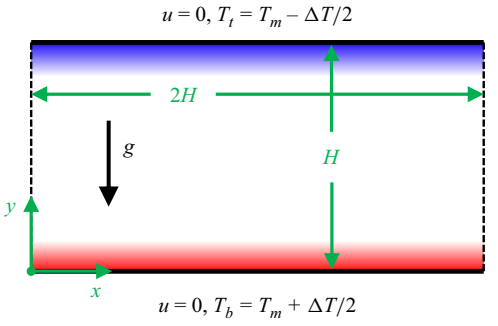

Figure 2. Schematic diagram of the flow configuration, where H is the height of the RBC cell, g is the acceleration due to gravity, ΔT is the temperature difference between the top and bottom plates, T_m is the mean temperature, and T_t and T_b are the temperatures at the top and bottom plates, respectively. Solid lines represent the no-slip boundary conditions. Dashed lines represent the periodic boundary conditions.

Considering that LBM exhibits second-order accuracy in both time and space, we employ a second-order Runge–Kutta scheme for temporal discretization and a second-order central difference scheme for spatial discretisation. In this study, we focus on the effects of compressibility on RBC. Thus, we set ν, c_v and λ as constants with values 0.1, 5 and 1, respectively. Meanwhile, the gravity is set to $g = 0.0001$ unless otherwise noted. Figures 1(b) and 1(c) show the variation of c_p and $Pr = \rho c_p \nu/\lambda$ with temperature for various pressures, respectively.

2.4. *Boundary conditions*

Considering the roll period near the onset of RBC is $2.016H$ for an infinite aspect ratio (Clever & Busse 1974; Shan 1997), we selected a computational domain with an aspect ratio of 2, corresponding to a roll period of $2H$. The schematic diagram of the flow configuration is shown in figure 2. Periodic boundary conditions were applied on the sides. This approach, with a roll period of $2H$ and periodic boundary conditions, is well established in the literature (Furukawa & Onuki 2002; Johnston & Doering 2009; Winchester *et al.* 2022). The specific boundary conditions are as follows. The top and bottom plates are set as no-slip boundary conditions using Zou–He boundary scheme (Zou & He 1997).

Top plate:

$$f_4 = f_2, \tag{2.20}$$

$$f_7 = f_5 + \frac{(f_1 - f_3)}{2} + \frac{\delta_t \left(F_x + F_y\right)}{4}, \tag{2.21}$$

$$f_8 = f_6 - \frac{(f_1 - f_3)}{2} - \frac{\delta_t \left(F_x - F_y\right)}{4}. \tag{2.22}$$

Bottom plate:

$$f_2 = f_4, \tag{2.23}$$

$$f_5 = f_7 - \frac{(f_1 - f_3)}{2} - \frac{\delta_t \left(F_x + F_y\right)}{4}, \tag{2.24}$$

$$f_6 = f_8 + \frac{(f_1 - f_3)}{2} + \frac{\delta_t \left(F_x - F_y\right)}{4}. \tag{2.25}$$

The top plate is maintained at a constant temperature $T_t = T_m - \Delta T/2$, while the bottom plate is set at $T_b = T_m + \Delta T/2$. At this point, T_m is the arithmetic mean value of the top and bottom plates' temperatures, and ΔT is the temperature difference between the top and bottom plates. Initially, both density and temperature are set to their mean values, with a temperature perturbation introduced at the centre of the domain. As shown in figure 1, fluid compressibility increases as the system approaches the critical point, leading to a corresponding rise in the peak of c_p. The stronger the compressibility, the more pronounced the NOB-II effects. However, the sharp fluctuation of c_p also introduces NOB-I effects. To emphasise NOB-II effects while minimising the impact of NOB-I effects, the computational conditions in this paper are set to $p_m = 2p_{cr}$ and $T_m = 1.05T_{cr}$. The mean density ρ_m is calculated by substituting T_m and p_m into (2.14).

3. Model validation

3.1. *Static cavity*

We constructed a static cavity configuration to validate the capability of our model in simulating fluid compressibility. The only difference between this configuration and RBC is that the temperatures of the top and bottom plates are reversed – i.e. the bottom plate is cooled, and the top plate is heated. This set-up ensures that the fluid remains stationary throughout the simulation. Under these conditions, the density and pressure profiles are governed by the following equations:

$$\frac{\partial p}{\partial y} = \rho(p, T)g, \quad \frac{\partial p}{\partial x} = 0. \tag{3.1}$$

Figure 3 presents the density and pressure profiles of the static cavity under various conditions. Three simulation scenarios were set up: the first considers only the effect of gravity (black), the second considers only the effect of temperature (blue), and the third accounts for the effects of both temperature and gravity (red). The analytical solutions is obtained using the Euler method with a sufficiently small time step. The results demonstrate that the proposed model effectively captures the variation in density as a function of temperature and pressure. The computed results closely match the analytical solutions under all conditions, validating the model's capability to accurately simulate fluid compressibility.

3.2. *Schwarzschild criterion*

Giterman & Shteinberg (1970) proposed that the onset of RBC under NOB-II conditions should be determined using Schwarzschild criterion:

$$Ra = \frac{\rho c_p g \beta H^4}{\lambda \nu}\left(\frac{\Delta T}{H} - \frac{\beta g T}{c_p}\right) \geqslant Ra_c, \tag{3.2}$$

where Ra_c is the critical Rayleigh number for the Schwarzschild criterion, which equals 1708 for both rigid boundaries (Carlès & Ugurtas 1999). Based on this criterion, the temperature difference required for the onset of convection can be expressed as (Kogan *et al.* 1999)

$$\Delta T_{on} = \Delta T_R + \Delta T_{ad} = Ra_c \frac{\lambda \nu}{g \rho c_p \beta H^3} + \frac{g T \beta H}{c_p}. \tag{3.3}$$

The first term on the right-hand side represents the contribution from the Rayleigh criterion and the second term accounts for the effect of ATG.

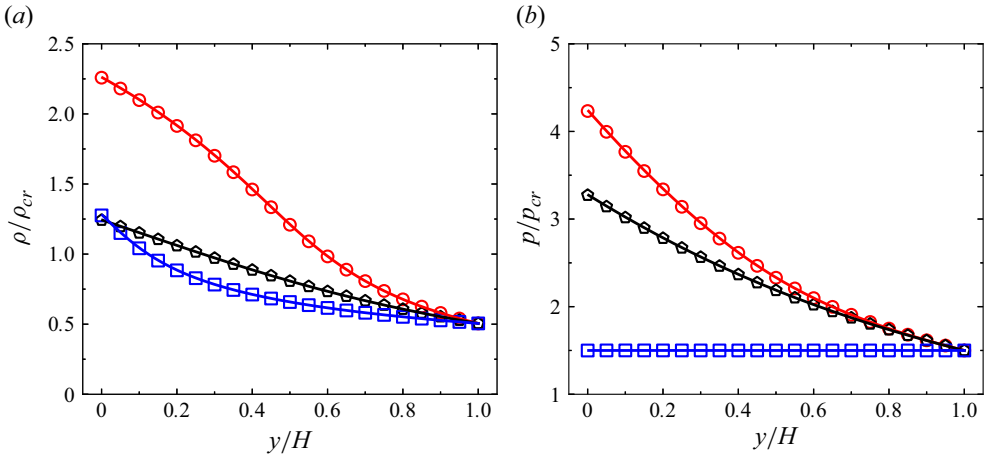

Figure 3. (*a*) Density and (*b*) pressure profiles of the static cavity under various conditions. Lines represent the analytical solutions. Points represent the calculated results using the presented LB model. In these cases, the cavity height is set to $H = 200$ and the pressure of top plate is set to $p(H) = 1.5p_{cr}$. Black lines and pentagon points represent the results for $T(y) = 1.25T_{cr}$ and $g = 0.00025$. Blue lines and square points represent the results for $T(y) = (1.05 + 0.2y/H)T_{cr}$ and $g = 0$. Red lines and circle points represent the results for $T(y) = (1.05 + 0.2y/H)T_{cr}$ and $g = 0.00025$.

We use the proposed LB model to determine the onset temperature difference for convection and validate it by comparing it with the Schwarzschild criterion. First, we compute ΔT_{on} according to the Schwarzschild criterion using (3.3). Then, we simulate the convective behaviour for ΔT values of $0.9\Delta T_{on}$, $0.95\Delta T_{on}$, $1.05\Delta T_{on}$, $1.1\Delta T_{on}$ and $1.15\Delta T_{on}$. Figure 4(*a*) illustrates the evolution of the spatial-averaged velocity $\langle|\boldsymbol{u}|\rangle_{x,y}$ over time. In the initial phase, similar oscillatory behaviour is observed across different ΔT due to the comparable nature of the introduced perturbations. However, when ΔT is less than ΔT_{on}, $\langle|\boldsymbol{u}|\rangle_{x,y}$ decreases steadily over time, indicating that convection initiated by the initial perturbation is unsustainable. At this point, Nu is equal to 1, representing pure heat conduction. When ΔT exceeds ΔT_{on}, $\langle|\boldsymbol{u}|\rangle_{x,y}$ stabilises at a certain value over time, enabling sustained convection. Meanwhile, as shown in figure 4(*a*), the steady-state $\langle|\boldsymbol{u}|\rangle_{x,y}$ increases with ΔT, indicating that greater temperature differences lead to greater convective intensity. The convective onset temperature difference is obtained by linearly fitting and extrapolating the Nu–ΔT relationship near the convective threshold (Yu *et al.* 2017). As shown in figure 4(*b*), we fit a line through the points where $Nu > 1$ and the intersection of this line with $Nu = 1$ is taken as the onset point of convection determined by LBM. Here, the Nusselt number Nu is defined as (Shishkina & Wagner 2016; Shishkina *et al.* 2016)

$$Nu = -\frac{H}{\Delta T}\left\langle\frac{\partial T}{\partial y}\right\rangle_w, \tag{3.4}$$

where $\langle\cdot\rangle_w$ denotes the mean value over the top and bottom plates.

Figure 5 compares the calculated results with the Schwarzschild criterion. The points represent the onset temperature difference ΔT_{on} obtained from the LB simulations, while the solid lines represent ΔT_{on} given by the Schwarzschild criterion. It can be seen that the calculated results are in close agreement with the Schwarzschild criterion, further validating the accuracy of our numerical model. The relationship between ΔT_{on} and H for various T_m is shown in figures 5(*a*)–5(*c*). When H is small, ΔT_R is the dominant

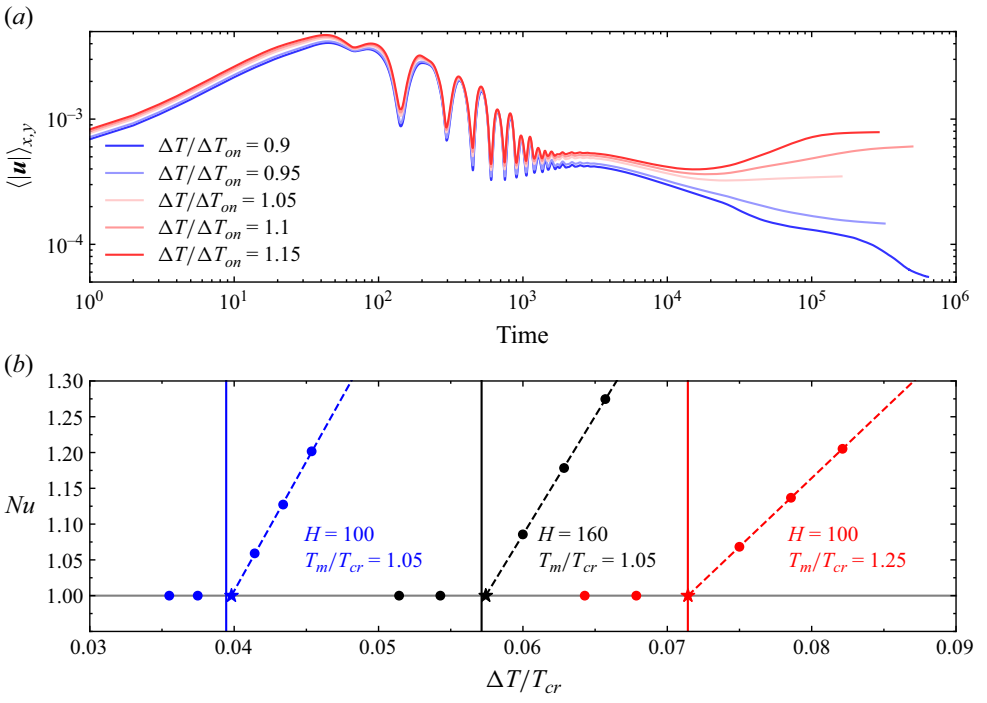

Figure 4. (*a*) Variation of the spatial-averaged velocity $\langle |\boldsymbol{u}| \rangle_{x,y}$ with time for various temperature difference ΔT at $H = 60$ and $T_m = 1.05T_{cr}$. (*b*) Variation of Nusselt number Nu with temperature difference ΔT under various conditions. The same colour represents the same conditions and corresponding parameters have been specified in the figure. The vertical solid lines is the convective onset temperature difference ΔT_{on} given by the Schwarzschild criterion. Five circle points under each condition represent the results calculated by LBM, from left to right the temperature difference is $0.9\Delta T_{on}$, $0.95\Delta T_{on}$, $1.05\Delta T_{on}$, $1.1\Delta T_{on}$ and $1.15\Delta T_{on}$. The dashed lines represent a linear fit to the last three points. Asterisk points represent the intersection of the dashed line with $Nu = 1$.

factor, decreasing at a rate of H^{-3} as H increases. In contrast, for large H, ΔT_{ad} becomes the dominant factor, increasing linearly with H. Thus, the onset temperature difference initially decreases and then increases as H increases. Figures 5(*d*)–5(*f*) depict the variation of ΔT_{on} with T_m. The results show that ΔT_R initially decreases and then increases as T_m rises, reaching a minimum near the pseudo-critical point. This behaviour is primarily attributed to the peak in c_p near the pseudo-critical point, as illustrated in figure 1(*b*). Conversely, ΔT_{ad} increases and then gradually decreases as T_m increases. The overall trend of ΔT_{on} is governed by the combined effects of ΔT_{ad} and ΔT_R. When H is small, the trend follows that of ΔT_R, whereas for large H, it aligns more closely with ΔT_{ad}.

3.3. *Experimental data*

In this section, we further validate our model using experimental data. Kogan *et al.* (1999) experimentally studied the RBC in supercritical ^{3}He. Figure 6 presents the experimental results, where Ra^* is defined as

$$Ra^* = \frac{Ra - Ra_c}{Ra_c}. \tag{3.5}$$

The results indicate that $j/(1-\alpha)$ follows a power-law relationship with Ra^*, with the best power-law fit expressed as $j/(1-\alpha) = 1.465(Ra^*)^{1.125}$. The definition of j is given

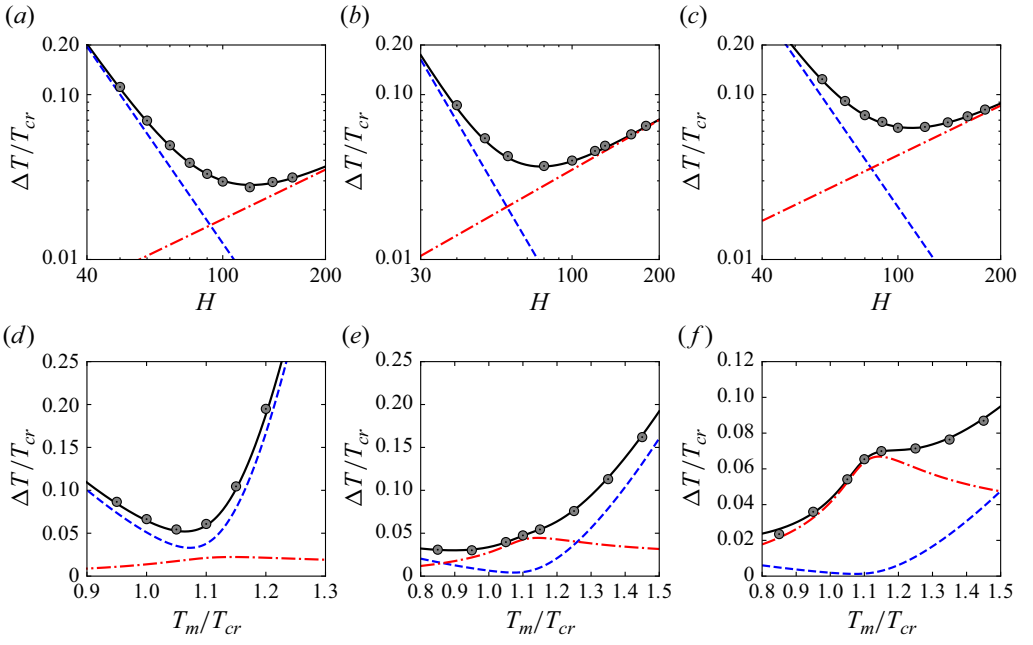

Figure 5. Effects of the (*a–c*) height H and (*d–f*) mean temperature T_m on the onset temperature difference. (*a*) $T_m = 0.95T_{cr}$, (*b*) $T_m = 1.05T_{cr}$, (*c*) $T_m = 1.2T_{cr}$, (*d*) $H = 50$, (*e*) $H = 100$, (*f*) $H = 150$. Circle points represent the calculated results of LBM. Black solid lines represent ΔT_{on}, which is obtained from the Schwarzschild criterion. Red dash-dotted lines represent ΔT_{ad}. Blue dashed lines represent ΔT_R.

by (Kogan *et al.* 1999)

$$j = (Nu - 1)(Ra^* + 1). \tag{3.6}$$

The parameter α represents the ratio of ΔT_{ad} to ΔT_{on}, which can effectively indicate the intensity of NOB-II effects, as will be shown later. The value of α ranges from 0 to 1, where $\alpha = 0$ corresponds to the standard RBC.

Figure 6 compares the best-fit curve from the experimental data with the results of LB simulations. The best power-law fit for the LB results is $j/(1-\alpha) = 1.517(Ra^*)^{1.116}$. The results of the LB simulations are in good agreement with the experimental data. The strong agreement between the two further validates our numerical model. It is worth noting that the definitions of the horizontal and vertical axes in figure 6 differ from those used by Kogan *et al.* (1999); however, they are equivalent, as demonstrated in Appendix A.

3.4. *OB-RBC*

The above comparisons validate the global parameters (e.g. Nu, ΔT_{on}). To further assess the accuracy of our model, we compare the calculated flow fields under weak NOB-II effects with those obtained from OB-RBC. Table 1 presents a comparison of simulation parameters and results. In our simulations, we have used a value of $\alpha \approx 0.06$ to represent weak NOB-II effects. The results of OB-RBC are calculated using the thermal lattice Boltzmann method presented by Gao *et al.* (2021) (denoted as OB model). The results show that the calculated results of OB-RBC closely align with the results reported by Clever & Busse (1974). The slight deviation observed in table 1 arises from the difference in Pr. Clever & Busse (1974) set Pr to 7.0, while in our calculations, we used a Pr value of 8.25, which corresponds to supercritical fluid at $T_m = 1.05T_{cr}$ and $p_m = 2p_{cr}$.

Ra	H	ΔT	α	$Nu_{C\&B}$	Nu_{ob}	Nu_{nob}	$Diff$
3000	80	0.0812	0.069	1.667	1.662	1.586	−4.6 %
5000	120	0.0789	0.053	2.112	2.102	2.000	−4.9 %
10 000	150	0.0816	0.064	2.618	2.606	2.493	−4.3 %

Table 1. Comparation of the calculated results. The columns from left to right indicate the following: the Rayleigh number Ra, the height of the RBC cell H, the temperature difference ΔT, the ratio of adiabatic temperature gradient to the temperature difference α, the Nusselt number calculated by Clever & Busse (1974) $Nu_{C\&B}$, the Nusselt number calculated by the OB model Nu_{ob}, the Nusselt number calculated by our model Nu_{nob}, and the deviation between the results of the OB model and our model $Diff = (Nu_{nob} - Nu_{ob})/Nu_{ob}$.

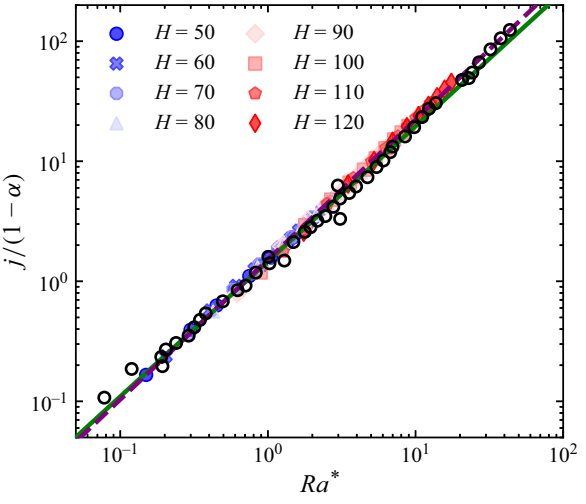

Figure 6. Variation of $j/(1-\alpha)$ with Ra^* for various H. Hollow points represent experimental data of Kogan *et al.* (1999). Solid points are the calculated results of LBM for various H. The green solid line, $j/(1-\alpha) = 1.465(Ra^*)^{1.125}$, is the best power-law fit to the experimental data. The purple dashed line, $j/(1-\alpha) = 1.517(Ra^*)^{1.116}$, is the best power-law fit to the results of LB simulations.

Under the weak NOB-II effects, the Nusselt number (Nu) calculated by our model is slightly smaller than that obtained from OB-RBC, with a deviation within 5 %. This discrepancy is considered acceptable and further validates our model. The underlying reasons for this deviation will be discussed in detail in § 4.4.

For better comparison, we define the normalised temperature as follows:

$$\widetilde{T} = \frac{T - T_m}{T_b - T_t}. \tag{3.7}$$

The normalised temperature ranges from −0.5 to 0.5, where the bottom plate is fixed at 0.5 and the top plate is fixed at −0.5. The reduced velocity is defined as

$$\widetilde{u}_y = \frac{u_y H \rho}{\nu \rho_m}. \tag{3.8}$$

Figures 7(*a*) and 7(*b*) compare the flow fields obtained from the OB model with those from our model. It can be observed that the temperature and velocity fields calculated by our model under weak NOB-II effects show a strong agreement with those of the OB model. Figures 7(*c*) and 7(*d*) provide further comparison of the horizontal-averaged temperature

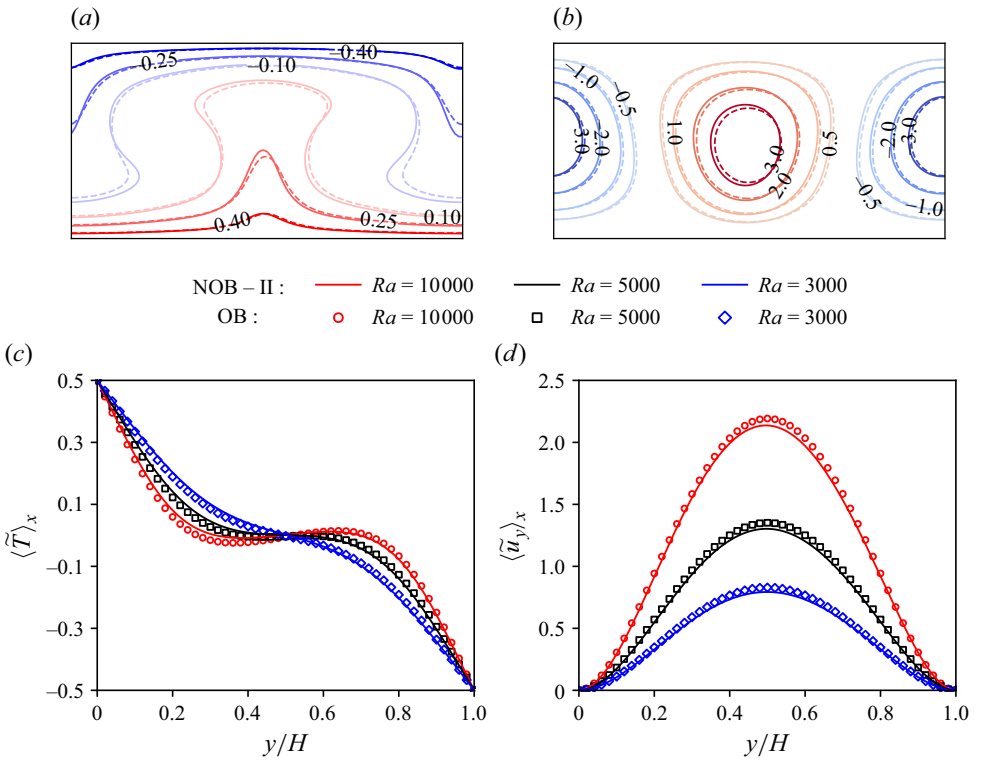

Figure 7. (*a,b*) Normalised (*a*) temperature $\widetilde{T}$ and (*b*) reduced velocity $\widetilde{u}_y$ contours for $Ra = 10\,000$. Solid lines represent the results of the OB model. Dashed lines represent the results of our model. (*c,d*) Horizontal-averaged (*c*) temperature $\langle \widetilde{T} \rangle_x$ and (*d*) velocity $\langle \widetilde{u}_y \rangle_x$ profiles for various Ra. Solid lines represent the results of our model. Points represent the results of the OB model.

and velocity profiles calculated by both models, with results again demonstrating good agreement. Overall, the calculations from our model are in close alignment with those of the OB model under weak NOB-II effects. The deviation induced by the NOB-II effect remains within an acceptable range, which serves to fully validate our model. The differences in the results of the two models due to the NOB-II effect will be discussed in detail in § 4.

4. Results and disscussion

4.1. *Symmetry*

First, we examine whether NOB-II effects disrupt temperature symmetry in the same way as NOB-I effects. Figure 8(*a*) shows the horizontal-averaged normalised temperature, $\langle \widetilde{T} \rangle_x$, as a function of y/H for various temperature differences. The results indicate that the overall symmetry of the temperature profile remains intact. All curves pass through the point (0.5, 0) without significant deviation as the temperature difference increases. We further present the variation of the normalised mean temperature of central plane $\widetilde{T}_c$ with α in figure 8(*b*). The results show that $\widetilde{T}_c$ fluctuates within a narrow range of ± 0.01. Previous studies on the NOB-I effects have reported deviations in $\widetilde{T}_c$ as follows: $+0.05 - +0.17$ for glycerol (Zhang *et al.* 1997), $0 - +0.08$ for water (Ahlers *et al.* 2006; Sugiyama *et al.* 2009; Demou & Grigoriadis 2019), $0 - +0.05$ for air

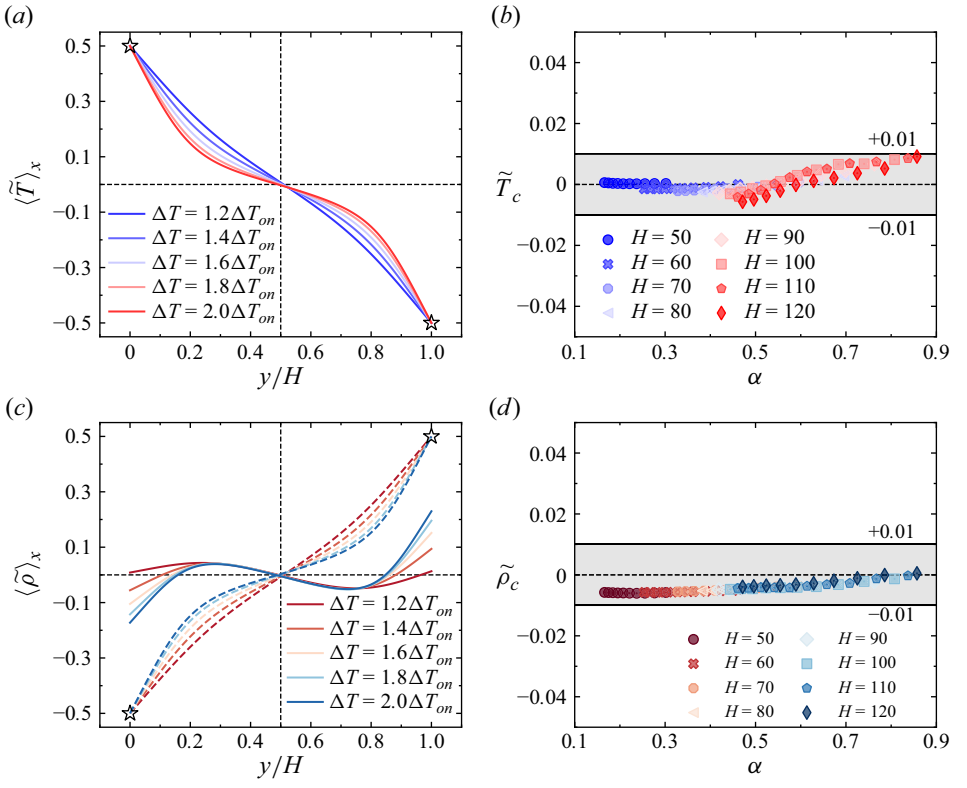

Figure 8. (*a*) Horizontal-averaged normalised temperature $\langle\widetilde{T}\rangle_x$ as a function of y/H for various ΔT at $H = 100$. (*b*) Variation of the normalised temperature of centre plane $\widetilde{T}_c$ with α for various H. (*c*) Horizontal-averaged normalised density $\langle\widetilde{\rho}\rangle_x$ as a function of y/H for various ΔT at $H = 100$. Dashed lines represent the result of (4.2) $\widetilde{\rho} = -\widetilde{T}$. (*d*) Variation of the normalised centre plane density $\widetilde{\rho}_c$ with α for various H. Ten data points for each H represent varying ΔT values, specifically from 1.1 to $2.0\Delta T_{on}$ in increments.

(Wan *et al.* 2020), $-0.22- + 0.08$ for supercritical SF_6 (Yik *et al.* 2020) and $-0.035- + 0.02$ for supercritical ethane (Ahlers *et al.* 2007, 2008). Additionally, these studies consistently show that the deviation increases with the intensity of NOB-I effects. In contrast, the deviations observed in figure 8(*b*) are minimal (<0.01) and show no clear trend. Therefore, we conclude that the NOB-II effects have no impact on $\widetilde{T}_c$, meaning that NOB-II effects do not affect $\widetilde{T}_c$ and thus do not break the temperature symmetry. The slight fluctuations in $\widetilde{T}_c$ are most likely caused by minor variations in c_p and β with temperature (see figure 1), which are attributable to the NOB-I effects.

Under OB and NOB-I conditions, the density in the buoyancy term decreases as temperature increases, maintaining a one-to-one correspondence. However, under NOB-II conditions, density is determined by both temperature and pressure, making the study of the density field particularly important (Amiroudine *et al.* 2001; Carlès & El Khouri 2001). To examine the density symmetry, we define the normalised density as follows:

$$\widetilde{\rho} = \frac{\rho - \rho_m}{\rho_m \beta \Delta T}, \tag{4.1}$$

Under OB conditions, $\widetilde{\rho}$ and $\widetilde{T}$ are related by the following equation:

$$\widetilde{\rho} = \frac{\rho - \rho_m}{\rho_m \beta \Delta T} = \frac{-\rho_m \beta (T - T_m)}{\rho_m \beta (T_b - T_t)} = -\widetilde{T}. \tag{4.2}$$

This implies that $\widetilde{\rho}$ and $\widetilde{T}$ have opposite signs under OB conditions. Figure 8(c) shows the variation of the horizontal-averaged normalised density distribution $\langle\widetilde{\rho}\rangle_x$ with y/H for various ΔT. The results indicate that the overall symmetry of the density profile remains intact. Figure 8(d) presents the variation of the normalised mean density at the centre plane $\widetilde{\rho}_c$ with α. The results show that $\widetilde{\rho}_c$ fluctuates within a narrow range of ± 0.01, with deviations of less than 0.01. This suggests that NOB-II effects do not break the density symmetry either. However, the profiles in figure 8(c) deviate significantly from the relationship described by (4.2). Therefore, it is necessary to further investigate the distribution of the density field, which is discussed in detail in § 4.2.

While studying the symmetry of temperature and density, values at the centre plane are of primary interest. In contrast, when analysing the symmetry of velocity under NOB conditions, the focus shifts to the velocity difference between the upper and lower regions (Horn *et al.* 2013). Under OB conditions, the velocity field is symmetric along the centre plane. However, under NOB conditions, this symmetry is disrupted. Experimental studies on NOB-I effects have revealed asymmetries in the upper and lower velocity fields (Valori *et al.* 2017). Therefore, it is essential to investigate the impact of NOB-II effects on the velocity field.

Figure 9(a) shows the variation of the horizontal-averaged absolute value of u_y with $|y/H - 0.5|$. Here, the horizontal coordinate is taken as $|y/H - 0.5|$ rather than y/H to emphasise the asymmetry between the upper and lower regions. The results indicate that the velocity field is asymmetric along the central horizontal plane, with $\langle|u_y|\rangle_x$ in the lower region consistently smaller than in the upper region. The relative deviation ε_u between the two regions is shown in figure 9(b), where ε_u is defined as follows:

$$\varepsilon_u = \frac{\langle|u_y|\rangle_{x,upper} - \langle|u_y|\rangle_{x,lower}}{\langle|u_y|\rangle_{x,y}}, \tag{4.3}$$

with the subscripts '*upper*' and '*lower*' representing the upper and lower regions, respectively. Figure 9(b) shows that the deviation between the two regions increases and then decreases with $|y/H - 0.5|$ and the maximum deviation increases with ΔT.

To further analyse the cause of this asymmetry, figure 9(c) presents the variation of the horizontal-averaged absolute value of ρu_y with y. This figure shows that momentum symmetry between the upper and lower regions is maintained, with minimal differences observed between the two regions. Figure 9(d) displays the relative deviation $\varepsilon_{\rho u}$, which is defined as follows:

$$\varepsilon_{\rho u} = \frac{\langle|\rho u_y|\rangle_{x,upper} - \langle|\rho u_y|\rangle_{x,lower}}{\langle|\rho u_y|\rangle_{x,y}}. \tag{4.4}$$

The results indicate that the momentum deviation remains within 0.02. In contrast, the maximum deviation in velocity is close to 0.1, as shown in figure 9(b). Thus, we conclude that under NOB-II conditions, the symmetry of momentum is preserved, while the asymmetry observed in the velocity field is attributed to variations in the density field.

4.2. *Density inversion*

Figure 10(a) presents the normalised density $\widetilde{\rho}$ contours at $\Delta T = 1.1\Delta T_{on}$ for various heights. In OB-RBC, it is widely accepted that the fluid at the bottom is less dense than at the top. Due to buoyancy, the lighter fluid rises, driving thermal convection. However, as H increases, leading to stronger NOB-II effects, the density field exhibits an intriguing

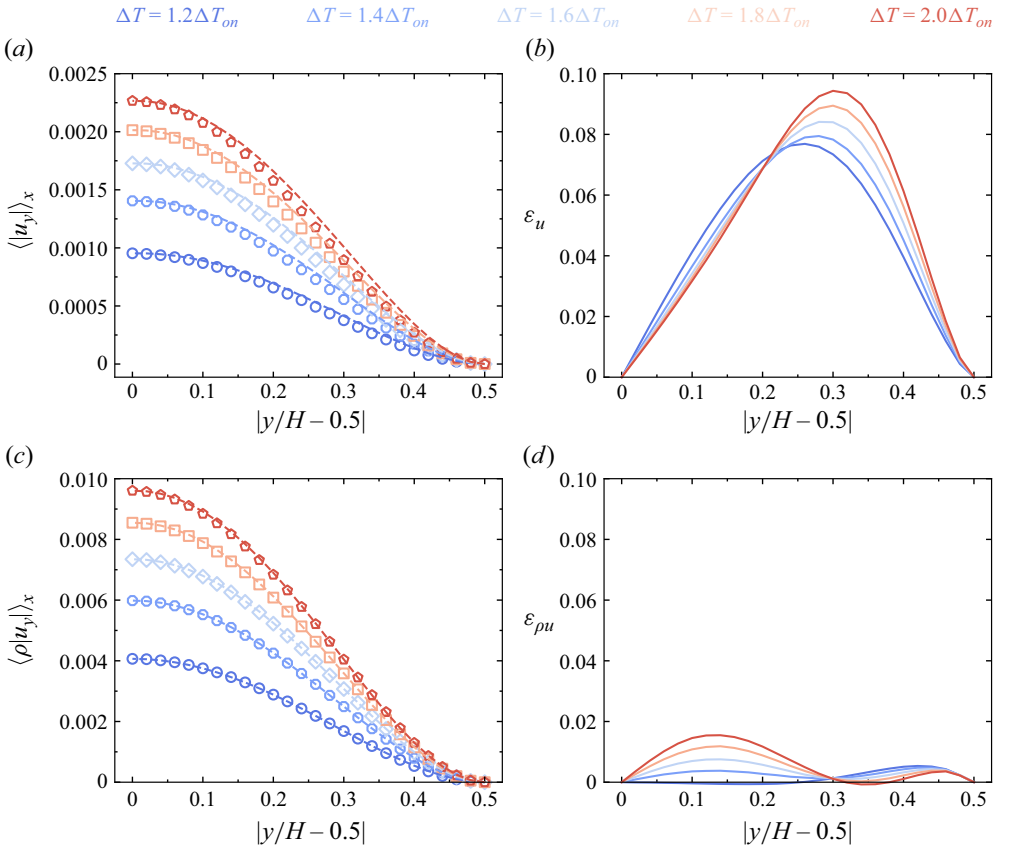

Figure 9. (*a*) Variation of the horizontal-averaged absolute value of u_y with $|y/H - 0.5|$ for various ΔT at $H = 100$. Dashed lines represent the results for the lower region ($y/H < 0.5$). Points represent the results for the upper region ($y/H > 0.5$). (*b*) Variation of the velocity deviation ε_u in the upper and lower regions with $|y/H - 0.5|$ for various ΔT at $H = 100$. (*c*) Variation of the horizontal-averaged absolute value of ρu_y with $|y/H - 0.5|$ for various ΔT at $H = 100$. (*d*) Variation of the momentum deviation $\varepsilon_{\rho u}$ in the upper and lower regions with $|y/H - 0.5|$ for various ΔT at $H = 100$.

inversion. As shown in figure 10(*a*), when $\alpha \leq 0.7$, the density remains higher at the top and lower at the bottom, consistent with OB-RBC behaviour. At this point, the contours for $\widetilde{\rho} = 0$ show a distribution of shapes that are convex upwards at the hot plume and concave downwards at the cold plume. However, when $\alpha \geqslant 0.81$, an inversion in the density field occurs, with the density becoming lower at the top and higher at the bottom. At this point, the contours for $\widetilde{\rho} = 0$ display shapes that are concave downwards in the hot plume and convex upwards in the cold plume.

We now examine the mechanism of density inversion, using hot plumes as a representative case (a similar analysis applies to cold plumes). Generally, density decreases with increasing temperature and increases with rising pressure. Due to fluid compressibility, the effect of pressure cannot be neglected. Although the fluid at the bottom is hotter, it is also subjected to higher pressure. As the hot plume ascends, its temperature decreases, which would typically increase its density. Simultaneously, the pressure also decreases, which tends to lower its density. When both the pressure gradient and fluid compressibility are significant, the effect of pressure on density outweighs the

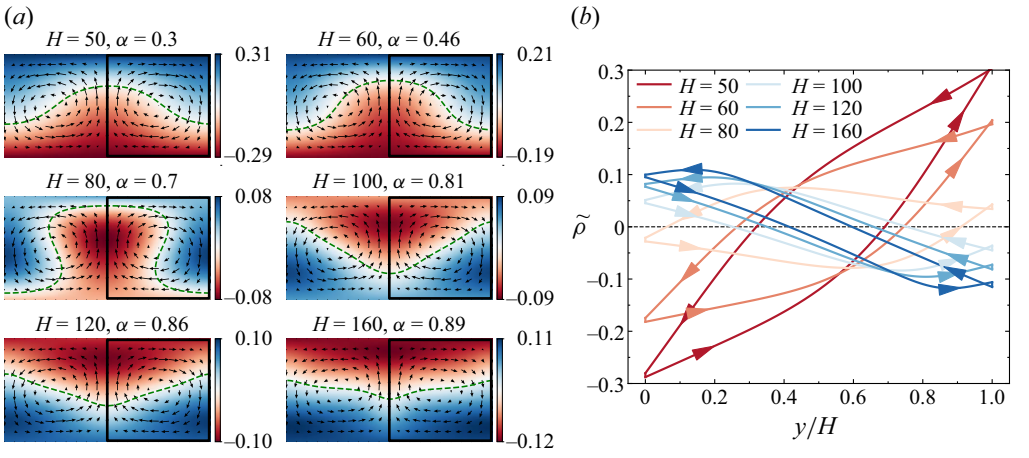

Figure 10. (*a*) Normalised density $\widetilde{\rho}$ contours at $\Delta T = 1.1\Delta T_{on}$ for various heights. Black arrows represent velocity vectors. The green dashed lines represent $\widetilde{\rho} = 0$. (*b*) Normalised density $\widetilde{\rho}$ distribution on the circulation lines (solid lines in panel *a*) for various heights.The arrows represent the direction of flow.

effect of temperature. Consequently, the density gradually decreases as the hot plume rises, leading to the phenomenon of density inversion.

Although the mechanism of density inversion is understood, it remains unclear how convection can persist when density inversion occurs. This is particularly intriguing, as it is generally accepted that a fluid is stable when its density increases with height. A typical example of this is the stable conduction stratification of penetrative RBC (Toppaladoddi & Wettlaufer 2018; Wang *et al.* 2019). To elucidate the mechanism of convection, figure 10(*b*) shows the normalised density distribution along the flow circulation lines (indicated by the solid lines in figure 10*a*). As shown in figure 10(*b*), the fluid density decreases with increasing height when H is large, further confirming the occurrence of density inversion. From figure 10(*b*), we observe a common feature in the density circulation lines: for all values of H, the fluid exhibits counterclockwise circulation on the ρ–y/H plot. This implies that, for a given y, the density of the rising hot plume is always lower than that of the sinking cold plume.

To better explain the flow mechanism when density inversion occurs, we schematically depict the flow structure of RBC in figure 11. As shown in figure 11(*a*) and 11(*b*), when density inversion is not present, the densities of both the hot and cold plumes increase as y increases. For a given y, the density of the hot plume is lower than that of the cold plume. When density inversion occurs, the densities of both the hot and cold plumes decrease as y increases. Meanwhile, for a given y, the density of the hot plume remains lower than that of the cold plume. We elaborate on the example of one cycle consisting of half a hot plume and half a cold plume, as is illustrated in figure 11(*c*). It can be seen in figure 10(*a*) that the flow velocity at the cycle centre is very low. Therefore, we can abstract the cycle as a natural circulation loop (Misale *et al.* 2007), with the dashed line at the centre of the loop representing the virtual boundary. For the natural circulation loop depicted in figure 10(*c*), the gravitational pressure drop on the left side is $\Delta p_1 = -\bar{\rho}_h g H$ and the gravitational pressure drop on the right side is $\Delta p_2 = \bar{\rho}_c g H$, where $\bar{\rho}_h$ and $\bar{\rho}_c$ represent the average densities of the hot and cold plumes, respectively. In addition, wall friction introduces a frictional pressure drop $\Delta p_3 = -\Delta p_f$, where Δp_f is positive. The total pressure drops is given by $\Delta p = (\bar{\rho}_c - \bar{\rho}_h) g H - \Delta p_f$. It is well known that, for a steady-state natural circulation loop, the net pressure drop must be zero. From the above analysis, we observe

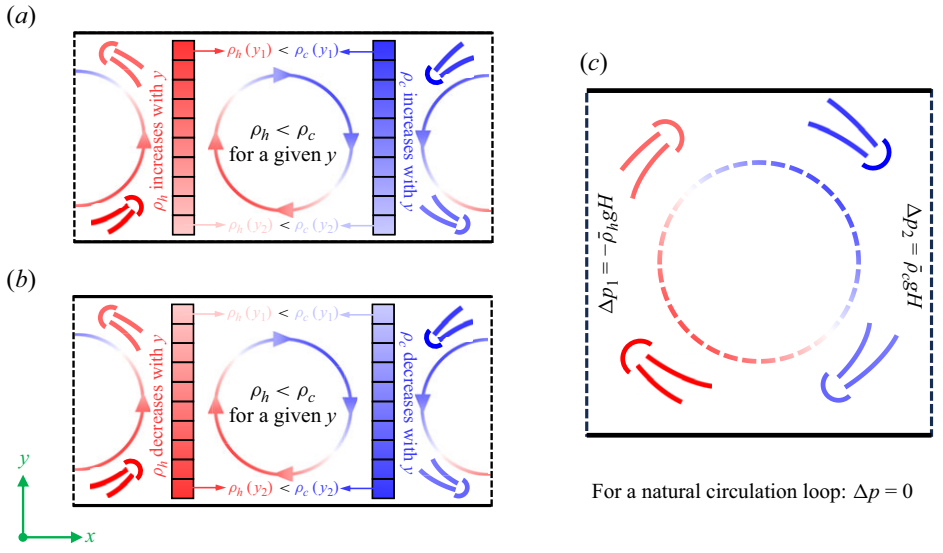

Figure 11. (*a*) Schematic of the flow structure and density distribution when the density field is not inverted. (*b*) Schematic of the flow structure and density distribution when the density field is inverted. (*c*) Schematic of one cycle consisting of half a hot plume and half a cold plume. ρ_h represents the density of the hot plume, ρ_c represents the density of the cold plume, and Δp_1 and Δp_2 represent the gravitational pressure drops on the left and right sides of the cycle, respectively.

that $\bar{\rho}_h$ is lower than $\bar{\rho}_c$. In this case, Δp can be equal to 0, allowing the circulation to persist. A similar analysis of the stable stratification in penetrative RBC reveals that, for a given y, $\bar{\rho}_h$ is always greater than $\bar{\rho}_c$. In this case, the total pressure drop is necessarily negative, and convection cannot persist.

To briefly summarise, under NOB-II conditions, the density of the hot plume is always less than that of the cold plume for a given y, regardless of whether density inversion occurs. The buoyancy difference due to the density difference between the two drives the convection to persist. The flow mechanism is very similar to a natural circulation loop.

4.3. *Condition for density inversion*

Building on our understanding of the convective mechanism, we now seek to identify the conditions under which density inversion occurs. To this end, we define the normalised density difference:

$$\Delta\widetilde{\rho} = \widetilde{\rho}_t - \widetilde{\rho}_b = \frac{\rho_t - \rho_b}{\rho_m \beta \Delta T}. \tag{4.5}$$

where ρ_b and ρ_t represent the mean densities of the bottom and top plates, respectively. Apparently, $\Delta\widetilde{\rho}$ is equal to 1 under OB conditions and $\Delta\widetilde{\rho} < 0$ indicates the occurrence of density inversion. Density is determined by both temperature and pressure. Thus, the density difference $\Delta\rho$ arises from the effects of temperature and pressure. The density difference from temperature is given by

$$\Delta\rho_T = (T_t - T_b)\left(\frac{\partial\rho}{\partial T}\right)_p = \rho_m \Delta T \frac{1}{\rho_m}\left(\frac{\partial\rho}{\partial T}\right)_p = \rho_m \beta \Delta T. \tag{4.6}$$

The density difference from pressure can be expressed as

$$\Delta\rho_p = (p_t - p_b)\left(\frac{\partial\rho}{\partial p}\right)_T = \rho_m g H \left(\frac{\partial\rho}{\partial p}\right)_T. \tag{4.7}$$

Since the ρ, p and T satisfy equation of state (2.14), triple product rule exists (see Elliott & Lira 2012, (6.15)):

$$\left(\frac{\partial\rho}{\partial p}\right)_T \left(\frac{\partial p}{\partial T}\right)_\rho \left(\frac{\partial T}{\partial\rho}\right)_p = -1. \tag{4.8}$$

Thus, $\Delta\rho_p$ can be further expressed as

$$\Delta\rho_p = -\rho_m g H \left(\frac{\partial\rho}{\partial T}\right)_p \left(\frac{\partial T}{\partial p}\right)_\rho = -\rho_m^2 g H\beta \left(\frac{\partial T}{\partial p}\right)_\rho. \tag{4.9}$$

Considering (2.19), the adiabatic temperature difference can be written in the following form (Kogan *et al.* 1999; Meyer & Kogan 2002):

$$\Delta T_{ad} = \frac{gT\beta H}{c_p} = \rho_m g H \frac{T}{\rho_m^2 c_p}\left(\frac{\partial\rho}{\partial T}\right)_p \left(\frac{\partial p}{\partial T}\right)_\rho \left(\frac{\partial T}{\partial p}\right)_\rho = \rho_m g H \frac{c_p - c_v}{c_p}\left(\frac{\partial T}{\partial p}\right)_\rho. \tag{4.10}$$

Thus, $\Delta\rho_p$ can also be expressed as

$$\Delta\rho_p = -\frac{c_p}{c_p - c_v}\rho_m\beta\Delta T_{ad} = -\frac{c_p}{c_p - c_v}\Delta\rho_{ad}, \tag{4.11}$$

where $\Delta\rho_{ad}$ is the density difference from ATG. We assume that the effects of temperature and pressure on the density difference are independent of each other. At this point, the normalised density difference can be expressed as

$$\Delta\widetilde{\rho} = \frac{\Delta\rho_T + \Delta\rho_p}{\rho_m\beta\Delta T} = 1 - \frac{c_p}{c_p - c_v}\alpha. \tag{4.12}$$

We present both our theoretical results (4.12) and the calculated data in figure 12. Notably, the calculated data closely align with the predictions of (4.12). They both show that the condition for density inversion is $\alpha > (c_p - c_v)/c_p$. Furthermore, (4.10) indicates that the precondition for density inversion is the inability of the density difference from ATG to fully counterbalance the density difference from pressure. From (4.6) and (4.11), the following equation can also be derived:

$$\alpha = \frac{\Delta T_{ad}}{\Delta T_{on}} = \frac{\Delta\rho_{ad}}{\Delta\rho_T} = -\frac{c_p - c_v}{c_p}\frac{\Delta\rho_p}{\Delta\rho_T}. \tag{4.13}$$

This indicates that α is proportional to the ratio of the density difference from pressure to that from temperature. The above analyses suggest that α does indicate the intensity of NOB-II effects well.

4.4. *Nusselt number*

Next, we analyse the impact of NOB-II effects on heat transfer. Figure 13(a) illustrates the variation of the Nusselt number Nu with Rayleigh number Ra. The results clearly show that NOB-II effects deteriorate the heat transfer, as Nu is consistently lower than that of OB-RBC for a given Ra. Additionally, for a given Ra, the larger the H, the smaller the Nu. We also calculated Nu of OB-RBC across various Ra using the thermal lattice Boltzmann

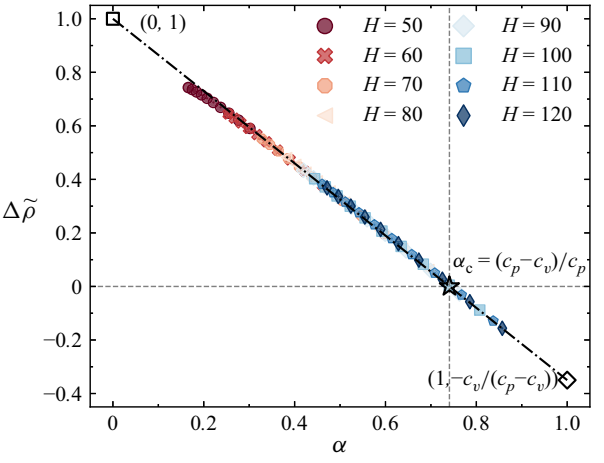

Figure 12. Variation of the normalised density difference between the top and bottom plates $\Delta\widetilde{\rho}$ with α for various heights. The dash-dotted line represents the theoretical prediction of (4.12). Ten data points for each H represent varying ΔT values, specifically from 1.1 to $2.0\Delta T_{on}$ in increments.

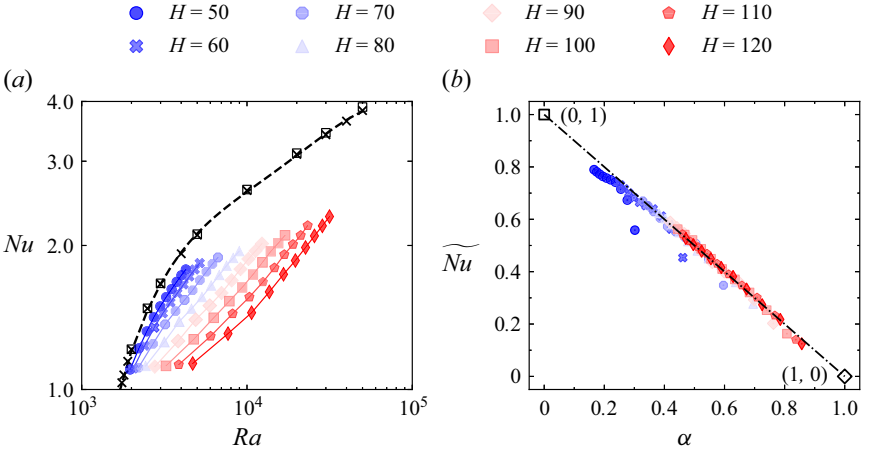

Figure 13. (*a*) Variation of Nusselt number Nu with Rayleigh number Ra for various H. Black square points represent the results of OB-RBC from Clever & Busse (1974). Black cross points represent the calculated results of OB-RBC using the thermal lattice Boltzmann method presented by Gao *et al.* (2021). Dashed line is the best fitting of black cross points. (*b*) Variation of normalised Nusselt number $\widetilde{Nu}$ with α for various H. Ten data points for each H represent varying ΔT values, specifically from 1.1 to $2.0\Delta T_{on}$ in increments.

method presented by Gao *et al.* (2021). The results show that the calculated results closely align with the results reported by Clever & Busse (1974). The slight deviation observed in figure 13(*a*) arises from the difference in Pr. Clever & Busse (1974) set Pr to 7.0, while in our calculations, we used a Pr value of 8.25, which corresponds to supercritical fluid at $T_m = 1.05T_{cr}$ and $p_m = 2p_{cr}$. Previous studies by Clever & Busse (1974) have already indicated that Nu decreases slightly with increasing Pr when $Pr > 2$.

To further quantify the heat transfer deterioration, we define the normalised Nusselt number as follows:

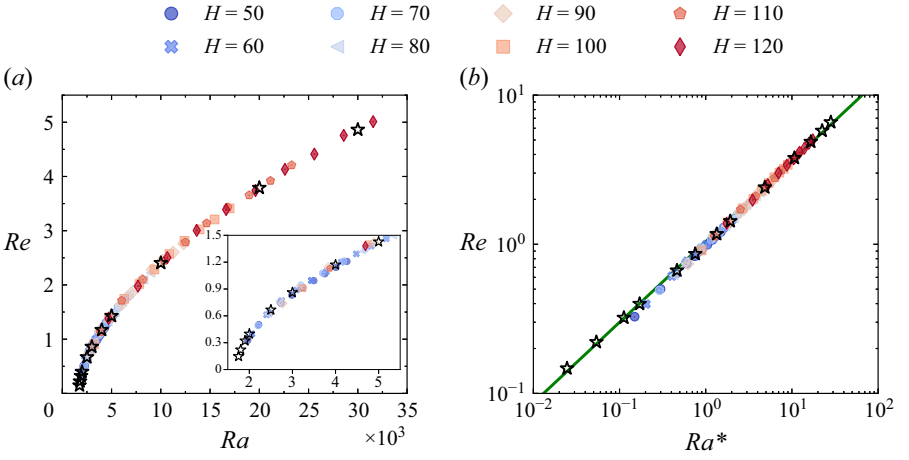

Figure 14. (*a*) Variation of Reynolds number Re with Rayleigh number Ra for various height H. (*b*) Variation of Reynolds number Re with reduced Rayleigh number Ra^* for various height H. Black asterisk points represent the calculated results of OB-RBC using the thermal lattice Boltzmann method presented by Gao *et al.* (2021). The solid line $Re = 1.042(Ra^*)^{0.541}$ is the best power-law fit to asterisk points. Ten data points for each H represent varying ΔT values, specifically from 1.1 to $2.0\Delta T_{on}$ in increments.

$$\widetilde{Nu} = \frac{Nu - 1}{Nu_{ob} - 1}, \tag{4.14}$$

where Nu_{ob} is the Nusselt number for the same Ra under OB conditions, obtained by fitting the black cross points in figure 13(*a*). The variation of $\widetilde{Nu}$ with α for various heights is shown in figure 13(*b*). The results indicate that the points fall nicely on the line $\widetilde{Nu} = 1 - \alpha$. This demonstrates that as α increases from 0 to 1, Nu decreases linearly from Nu_{ob} to 1, indicating significant heat transfer deterioration. Additionally, this further confirms that α is a reliable indicator of NOB-II intensity. Notably, several blue outliers are observed in figure 13(*b*), which primarily arise from the proximity of their Ra to Ra_c. This near-critical condition results in Nu_{ob} approaching unity, thereby causing the denominator in (4.14) to approach zero and consequently amplifying numerical uncertainties.

4.5. *Reynolds number*

We use the Reynolds number Re to indicate the convective intensity and Re is defined as follows (Shishkina & Wagner 2016):

$$Re = \frac{UH}{\nu}, \quad U = \sqrt{\langle \boldsymbol{u} \cdot \boldsymbol{u} \rangle_{x,y}}, \tag{4.15a,b}$$

where $\langle \cdot \rangle_{x,y}$ denotes the spatial average over the x and y directions, U represents the characteristic velocity. Figure 14(*a*) shows the variation of Re with Ra for various H. The results indicate that Re increases with Ra. Meanwhile, H has no impact on the relation between Re and Ra, as all points under both OB and NOB-II conditions fall on the same curve. Figure 14(*b*) shows the variation of Re with Ra^*. Under OB and NOB-II conditions, all points follow the same power-law relationship $Re = 1.042(Ra^*)^{0.541}$, further confirming the above conclusion.

Combined with the discussion in § 4.4, we observe a unique phenomenon: under dominant NOB-II effects, despite the persistence of vigorous convection, the heat transfer efficiency decreases to a level comparable to pure heat conduction. In other words, as α

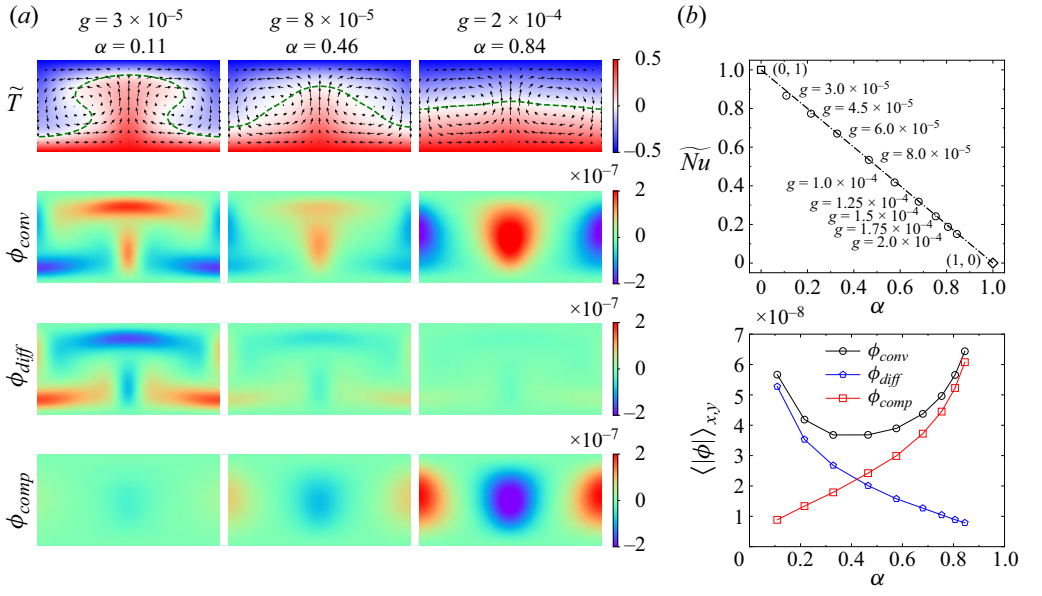

Figure 15. (*a*) Normalised temperature $\widetilde{T}$, convection item ϕ_{conv}, diffusion item ϕ_{diff} and compression work item ϕ_{comp} (from top to bottom panel) contours at $H = 100$ and $Ra = 10^4$ for various g. The green dashed lines represent $\widetilde{T} = 0$. (*b*) Variation of normalised Nusselt number $\widetilde{Nu}$ with α. The corresponding g is indicated in the figure. (*c*) Variation of the spatial-averaged of the absolute value of source term $\langle|\phi|\rangle_{x,y}$ with α. Black circle points represent the results of ϕ_{conv}. Blue pentagon points represent the results of ϕ_{diff}. Red square points represent the results of ϕ_{comp}. Connect points with lines for visual enhancement.

approaches 1, convection ceases to enhance heat transfer relative to pure conduction. The mechanism underlying this significant HTD urgently needs to be explored.

4.6. *Mechanism behind heat transfer deterioration*

To understand the mechanism behind HTD resulting from NOB-II effects, we first analyse the temperature field. As shown in figure 15(*a*), as α increases, the convective intensity remains essentially unchanged, as reflected by the arrows. However, the temperature distribution becomes progressively flatter as α increases. When $\alpha = 0.84$, the temperature distribution closely resembles that of pure heat conduction, characterised by a zero gradient in the x-direction and a linear decrease in the y-direction. At this point, HTD is observed, as shown in figure 15(*b*). This suggests that an unknown mechanism is absorbing the heat carried by the hot plume, thereby reducing its ability to transport heat to the top plate. We further investigate this mechanism by examining the energy conservation equation, which is given by

$$\frac{\partial T}{\partial t} = \underbrace{-\boldsymbol{u}\cdot\nabla T}_{\phi_{conv}} + \underbrace{\frac{1}{\rho c_p}\nabla\cdot(\lambda\nabla T)}_{\phi_{diff}} + \underbrace{\frac{1}{\rho c_p}\left(\frac{\partial \ln\rho}{\partial \ln T}\right)_p \frac{\mathrm{d}p}{\mathrm{d}t}}_{\phi_{comp}}, \tag{4.16}$$

where $\mathrm{d}p/\mathrm{d}t = \partial p/\partial t + \boldsymbol{u}\cdot\nabla p$ and (4.16) is equivalent to (2.18) (Moukalled *et al.* 2016). Here, the first term on the right-hand side represents convection term (ϕ_{conv}), the second term represents diffusion term (ϕ_{diff}) and the third term represents compression work term (ϕ_{comp}), which is ignored under OB conditions (Johnston & Doering 2009).

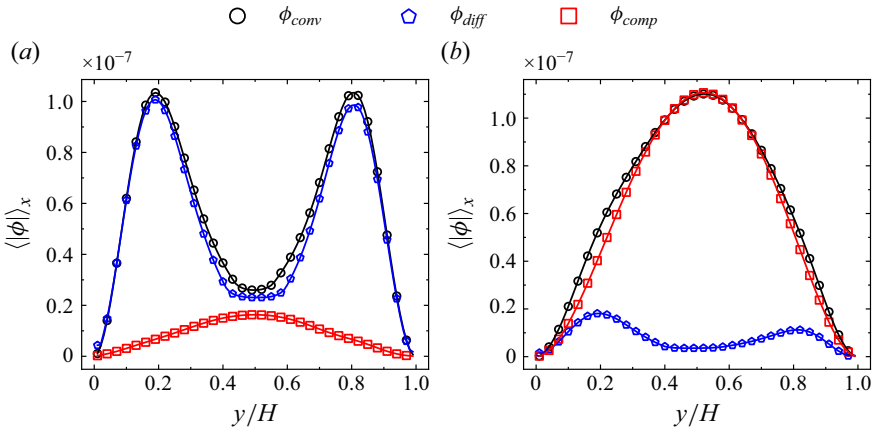

Figure 16. Variation of the horizontal-averaged of the absolute value of source term $\langle|\phi|\rangle_x$ with y/H for (*a*) $g = 3 \times 10^{-5}$ and (*b*) $g = 2 \times 10^{-4}$ at $H = 100$ and $Ra = 10^4$. Black circle points represent the results of ϕ_{conv}. Blue pentagon points represent the results of ϕ_{diff}. Red square points represent the results of ϕ_{comp}. Connect points with lines for visual enhancement.

Figure 15(*c*) shows the spatial-averaged of the absolute value of ϕ, $\langle|\phi|\rangle_{x,y}$, as a function of α. The results indicate that $\langle|\phi_{diff}|\rangle_{x,y}$ decreases with increasing α, while $\langle|\phi_{comp}|\rangle_{x,y}$ increases with increasing α. The contours of ϕ in figure 15(*a*) reveal that when NOB-II effects are weak, the diffusion and convection terms dominate and the compression term is negligible. This observation is consistent with figures 15(*c*) and 16(*a*). Since the diffusion term is related to the temperature gradient, it primarily acts near the plates, where the temperature gradient is the largest (Demou & Grigoriadis 2019; Wan *et al.* 2020), as shown in figure 8(*a*). Therefore, $\langle|\phi_{conv}|\rangle_x$ and $\langle|\phi_{diff}|\rangle_y$ present two peaks at the region near the plates, as shown in figure 16(*a*). At this point, the heat transfer mechanism is that the thermal plume carries the hot fluid near the bottom plate to the top, and then the heat of thermal plume is transfered to the top plate by thermal diffusion. This heat transfer mechanism enables the transfer of heat from the top plate to the bottom plate.

In contrast, when NOB-II effects are strong, the compression and convection terms dominate, while the diffusion term is negligible, as shown in figures 15(*a*), 15(*c*) and 16(*b*). According to (4.16), the compression work term is related to $\boldsymbol{u} \cdot \nabla p$. Although the pressure gradient is uniform throughout the domain ($\nabla p \approx \rho \boldsymbol{g}$), the velocity is higher in the central region and lower near the plates. Additionally, the velocity of the plume in the central region is parallel to the pressure gradient, whereas near the plates, it is perpendicular to the pressure gradient, as shown by the velocity vectors in figure 15(*a*). As a result, the compression term is larger in the central region and smaller near the plates, as illustrated in figures 15(*a*) and 16(*b*). At this point, the heat transfer mechanism changes: when thermal plumes transport hot fluid from the bottom plate to the top plate, the heat of thermal plume is absorbed in the central region by the compression work term. By the time the heat plume reaches the top, its temperature is significantly reduced, greatly reduceing its ability to transfer heat to the top plate. Consequently, the overall heat transfer from the bottom plate to the top plate is significantly impaired.

It is important to clarify that the previous mention of 'the compressible work term absorbing heat' is a metaphorical expression. In reality, the flow of fluid along in the opposite direction of the pressure gradient will lead to expansion, and the decrease in temperature during this process is a fundamental characteristic of compressible fluids.

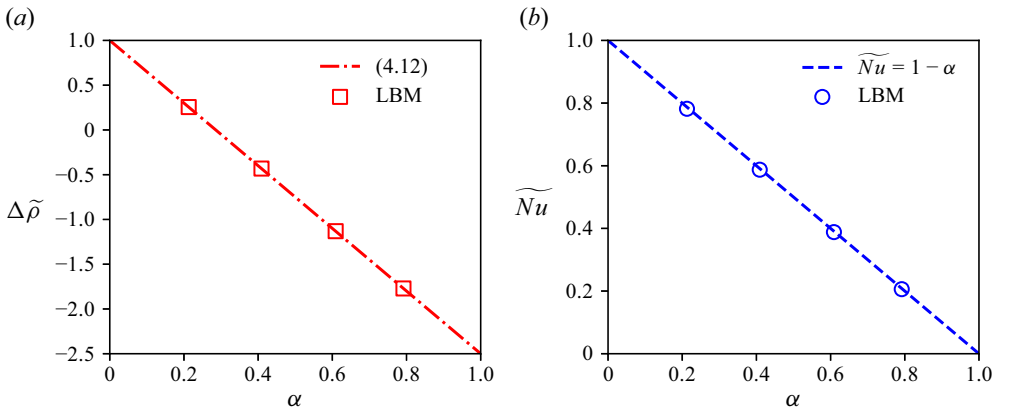

Figure 17. (*a*) Variation of the normalised density difference $\Delta\widetilde{\rho}$ with α for $Ra = 5000$. (*b*) Variation of the normalised Nusselt number $\widetilde{Nu}$ with α for $Ra = 5000$. The four points in each panel, from left to right, correspond to g: 2×10^{-4}, 3.2×10^{-4}, 4.8×10^{-4} and 7.5×10^{-4}.

4.7. *Perfect gas*

The above analysis and discussion pertain to supercritical fluids. However, our analysis is applicable to any compressible fluid. In this section, we perform simulations for a perfect gas to demonstrate the generalisability of our conclusions. The equation of state for a perfect gas is $p = \rho RT$. To align with the physical properties of air at room temperature, we take the following values for the parameters: $R = 1.6$, $\nu = 0.05$, $c_v = 4$, $\lambda = 1.643$, $T_m = 0.15$ and $p_m = 1$. With these parameter choices, $c_p/c_v = 1.4$ and $Pr = 0.71$, which correspond to the typical physical properties of air at room temperature. The height of the computational domain in this section is set to 100. The intensity of NOB-II effects is modulated by adjusting the gravitational acceleration.

Figure 17 illustrates the variation of $\widetilde{Nu}$ and $\Delta\widetilde{\rho}$ with α. The results show that density inversion and HTD also occur in a perfect gas. The simulation results are consistent with the conclusions obtained for supercritical fluids. The density difference $\Delta\widetilde{\rho}$ satisfies (4.12) and $\widetilde{Nu}$ decreases from 1 to 0 with increasing α, which fully validates the universality of our conclusions for compressible fluids.

5. Outlook and closure

Although previous studies have reported the impact of NOB-I effects on the temperature symmetry and heat transfer, the impact of NOB-II effects on symmetry and heat transfer remains unclear. To address these gaps, we conduct LB simulations of Rayleigh–Bénard convection in supercritical fluids. The specific methodology and conclusions are outlined as follows.

(i) Methodology: we present an LB model capable of simulating supercritical fluids. This model uses the D2Q9 discrete velocity model and Peng–Robinson equation of state, which is introduced by considering the intermolecular forces proposed by Shan & Chen (1993, 1994). The energy equation is solved using finite difference method. The model is validated against static cavity, Schwarzschild criterion and experimental data of Kogan *et al.* (1999). The best power-law fit to the LB results is $j/(1-\alpha) = 1.517(Ra^*)^{1.116}$, which is consistent with the experimental data of

$j/(1-\alpha) = 1.465(Ra^*)^{1.125}$. This good agreement demonstrates the potential of LBM for simulating supercritical fluids.

(ii) Symmetry of the flow field: the normalised temperature of centre plane is between -0.01 and +0.01 and there is no clear trend with α. This implies that the unlike NOB-I effects, NOB-II effects do not cause symmetry breaking in temperature. Meanwhile, the normalised density of the centre plane is also between -0.01 and +0.01, indicating that the density field is also symmetric. However, we observe an asymmetry in the velocity. Upon analysis, it is found that the momentum are still symmetric between the upper and lower regions and that the asymmetry in the velocity is due to the difference in density between the upper and lower regions.

(iii) Density inversion: for the first time, we report that convection can still occur when the bottom fluid is denser than the top fluid, a phenomenon we term density inversion. The underlying mechanism behind density inversion is attributed to the coupling effect of significant pressure gradient and fluid compressibility. In general, the density decreases with temperature and increases with pressure. While the fluid at the bottom is hotter, it is also subjected to higher pressure due to greater depth. Under significant NOB-II effects, the pressure effect dominates, causing the bottom fluid to have a higher density than the top, leading to density inversion. Meanwhile, both theoretical analyses and LB simulations confirm that the normalised density difference $\Delta\widetilde{\rho}$ and α satisfy a good linear relationship $\Delta\widetilde{\rho} = 1 - \alpha c_p/(c_p - c_v)$, indicating that the condition for density inversion is $\alpha > (c_p - c_v)/c_p$.

(iv) HTD: we observe that for a given Ra, NOB-II effects have no impact on Re. However, the Nusselt number decreases as α increases. The normalised Nusselt number and α satisfy a good linear relationship $\widetilde{Nu} = 1 - \alpha$. These results indicate that under dominant NOB-II effects, despite the persistence of vigorous convection, the heat transfer efficiency decreases to a level comparable to pure heat conduction, indicating significant HTD. The mechanism behind HTD is attributed to the compression work term in the energy equation, which absorbs heat from the hot plume in the central region, thereby reducing its capacity to transport heat from the bottom plate to the top.

The scope of the current study primarily focuses on laminar convective states. It remains an open question whether these conclusions hold under turbulent convective conditions. In future work, we aim to further optimise the LB model and develop corresponding code for 3-D turbulence simulations. This will enable an in-depth exploration of the impact of NOB-II effects on turbulent thermal 3-D convection.

Acknowledgements. We thank Chao Sun, Ying He, Ziyang Zhang, Wenxiang Fang and Haodong Yuan for helpful discussions and suggestions on the manuscript.

Funding. This work was supported by the Nuclear Power Technology Innovation Center of China (Grant No. HDLCXZX-2023-HD-013).

Declaration of interests. The authors report no conflict of interest.

Appendix A. Equivalence proof

In this appendix, we demonstrate that the definition of the horizontal and vertical axes in figure 6 is equivalent to that of the horizontal and vertical axes in figure 3 of Kogan *et al.* (1999). In the work of Kogan *et al.* (1999), the transverse coordinate is defined as

$$Ra^*_{corr} = \left(1 + \frac{Ra_R}{Ra_c}\alpha\right)\frac{Ra_R - Ra_{R,c}}{Ra_{R,c}}, \tag{A1}$$

where Ra_R is the Rayleigh number according to Rayleigh criterion, which is defined as

$$Ra_R = \frac{\rho c_p g \beta H^3 \Delta T}{\lambda \nu}. \tag{A2}$$

The vertical coordinate is defined as

$$j_{corr} = \left(1 + \frac{Ra_R}{Ra_c}\alpha\right) \frac{Ra_R(Nu-1)}{Ra_{R,c}}. \tag{A3}$$

According to (3.2) and (A2), when all parameters are the same except ΔT, we can derive

$$Ra = Ra_R(1-\alpha) = Ra_R\left(1 - \frac{\Delta T_{ad}}{\Delta T}\right), \tag{A4}$$

$$\frac{Ra_R(\Delta T_1)}{Ra_R(\Delta T_2)} = \frac{\Delta T_1}{\Delta T_2}, \tag{A5}$$

$$\frac{Ra_S(\Delta T_1)}{Ra_S(\Delta T_2)} = \frac{\Delta T_1 - \Delta T_{ad}}{\Delta T_2 - \Delta T_{ad}}. \tag{A6}$$

Thus, we can derive

$$\begin{aligned} Ra^*_{corr} &= \left(1 + \frac{Ra_R}{Ra_c}\alpha\right)\left(\frac{Ra_R}{Ra_{R,c}} - 1\right) \\ &= \left[1 + \frac{\Delta T}{\Delta T_c\,(1 - \Delta T_{ad}/\Delta T_c)}\frac{\Delta T_{ad}}{\Delta T}\right]\left(\frac{\Delta T}{\Delta T_c} - 1\right) \\ &= \frac{\Delta T_c}{\Delta T_c - \Delta T_{ad}}\left(\frac{\Delta T}{\Delta T_c} - 1\right) \\ &= \frac{\Delta T - \Delta T_c}{\Delta T_c - \Delta T_{ad}}, \end{aligned} \tag{A7}$$

$$Ra^* = \frac{Ra - Ra_c}{Ra_c} = \frac{\Delta T - \Delta T_{ad}}{\Delta T_c - \Delta T_{ad}} - 1 = \frac{\Delta T - \Delta T_c}{\Delta T_c - \Delta T_{ad}}. \tag{A8}$$

Thus, Ra^*_{corr} and Ra^* is proven to be equivalent.

$$\begin{aligned} j_{corr} &= \left(1 + \frac{Ra_R}{Ra_c}\alpha\right)\frac{Ra_R(Nu-1)}{Ra_{R,c}} \\ &= \left[1 + \frac{\Delta T}{\Delta T_c\,(1 - \Delta T_{ad}/\Delta T_c)}\frac{\Delta T_{ad}}{\Delta T}\right]\frac{\Delta T}{\Delta T_c}(Nu-1) \\ &= \frac{\Delta T_c}{\Delta T_c - \Delta T_{ad}}\frac{\Delta T}{\Delta T_c}(Nu-1) = \frac{\Delta T}{\Delta T_c - \Delta T_{ad}}(Nu-1), \end{aligned} \tag{A9}$$

$$\begin{aligned} \frac{j}{1-\alpha} &= \frac{(Nu-1)(Ra^*+1)}{1-\alpha} = (Nu-1)\frac{1}{1 - \Delta T_{ad}/\Delta T}\frac{Ra}{Ra_c} \\ &= (Nu-1)\frac{\Delta T}{\Delta T - \Delta T_{ad}}\frac{\Delta T - \Delta T_{ad}}{\Delta T_c - \Delta T_{ad}} \\ &= \frac{\Delta T}{\Delta T_c - \Delta T_{ad}}(Nu-1). \end{aligned} \tag{A10}$$

Thus, j_{corr} and $j/(1-\alpha)$ is proven to be equivalent.

Appendix B. Simulation parameters

Simulation parameters are given in tables 2, 3 and 4.

No.	H	$\Delta T/\Delta T_{on}$	α	$\widetilde{T}_c$	$\widetilde{\rho}_c$	$\Delta\widetilde{\rho}$	Ra	Nu	$\widetilde{Nu}$	Re
1	50	1.1	0.302	0	−0.006	0.59	1964	1.101	0.559	0.327
2	50	1.2	0.277	0	−0.006	0.621	2219	1.219	0.673	0.502
3	50	1.3	0.255	0	−0.006	0.647	2475	1.323	0.715	0.632
4	50	1.4	0.237	0	−0.006	0.669	2730	1.416	0.742	0.742
5	50	1.5	0.221	0	−0.006	0.687	2986	1.492	0.751	0.831
6	50	1.6	0.207	0	−0.006	0.703	3242	1.56	0.757	0.915
7	50	1.7	0.195	0	−0.006	0.716	3497	1.621	0.764	0.993
8	50	1.8	0.184	0	−0.006	0.726	3753	1.679	0.772	1.07
9	50	1.9	0.175	−0.001	−0.006	0.736	4009	1.732	0.781	1.141
10	50	2.0	0.166	−0.001	−0.006	0.743	4264	1.782	0.789	1.209
11	60	1.1	0.461	0	−0.005	0.379	2055	1.106	0.454	0.397
12	60	1.2	0.423	0.001	−0.005	0.43	2401	1.235	0.562	0.611
13	60	1.3	0.39	0.001	−0.005	0.473	2748	1.348	0.612	0.77
14	60	1.4	0.362	0.001	−0.006	0.509	3095	1.443	0.639	0.888
15	60	1.5	0.338	0.001	−0.006	0.54	3441	1.52	0.652	0.996
16	60	1.6	0.317	0.001	−0.006	0.567	3788	1.59	0.665	1.096
17	60	1.7	0.298	0.001	−0.006	0.591	4135	1.658	0.682	1.2
18	60	1.8	0.282	0.001	−0.006	0.611	4481	1.723	0.7	1.292
19	60	1.9	0.267	0.001	−0.006	0.629	4828	1.782	0.716	1.379
20	60	2.0	0.254	0.001	−0.006	0.644	5175	1.837	0.731	1.461
21	70	1.1	0.596	−0.001	−0.004	0.197	2205	1.111	0.348	0.491
22	70	1.2	0.547	0	−0.004	0.264	2701	1.246	0.448	0.755
23	70	1.3	0.505	0.001	−0.004	0.321	3198	1.368	0.507	0.946
24	70	1.4	0.469	0.001	−0.005	0.369	3695	1.458	0.53	1.079
25	70	1.5	0.437	0.001	−0.005	0.411	4191	1.539	0.552	1.212
26	70	1.6	0.41	0.002	−0.005	0.447	4688	1.612	0.573	1.343
27	70	1.7	0.386	0.002	−0.005	0.478	5185	1.693	0.604	1.476
28	70	1.8	0.364	0.002	−0.005	0.505	5681	1.763	0.629	1.592
29	70	1.9	0.345	0.002	−0.005	0.53	6178	1.83	0.652	1.698
30	70	2.0	0.328	0.002	−0.005	0.551	6675	1.888	0.67	1.791
31	80	1.1	0.695	−0.003	−0.002	0.063	2435	1.12	0.277	0.62
32	80	1.2	0.637	−0.001	−0.003	0.142	3161	1.256	0.359	0.937
33	80	1.3	0.588	0	−0.003	0.209	3888	1.386	0.424	1.16
34	80	1.4	0.546	0	−0.004	0.266	4615	1.475	0.45	1.323
35	80	1.5	0.51	0.001	−0.004	0.315	5341	1.56	0.479	1.496
36	80	1.6	0.478	0.001	−0.005	0.357	6068	1.649	0.515	1.68
37	80	1.7	0.45	0.002	−0.005	0.394	6795	1.735	0.549	1.836
38	80	1.8	0.425	0.002	−0.005	0.427	7522	1.814	0.579	1.978
39	80	1.9	0.403	0.002	−0.005	0.456	8248	1.883	0.603	2.097
40	80	2.0	0.382	0.002	−0.005	0.482	8975	1.946	0.623	2.223

Table 2. Simulation parameters. The columns from left to right indicate the following: the RBC cell height H, the reduced temperature difference $\Delta T/\Delta T_{on}$, the NOB-II parameter α, the normalised temperature of the centre plane $\widetilde{T}_c$, the normalised density of the centre plane $\widetilde{\rho}_c$, the normalised density difference $\Delta\widetilde{\rho}$, the Rayleigh number Ra, the Nusselt number Nu, the normalised Nusselt number $\widetilde{Nu}$ and the Reynolds number Re.

No.	H	$\Delta T/\Delta T_{on}$	α	$\widetilde{T}_c$	$\widetilde{\rho}_c$	$\Delta\widetilde{\rho}$	Ra	Nu	$\widetilde{Nu}$	Re
41	90	1.1	0.763	−0.007	−0.002	−0.028	2769	1.117	0.203	0.74
42	90	1.2	0.699	−0.005	−0.003	0.06	3830	1.263	0.293	1.146
43	90	1.3	0.645	−0.003	−0.003	0.133	4892	1.399	0.362	1.426
44	90	1.4	0.599	−0.001	−0.003	0.195	5953	1.497	0.399	1.632
45	90	1.5	0.559	−0.001	−0.004	0.249	7014	1.591	0.435	1.852
46	90	1.6	0.524	0.001	−0.004	0.296	8075	1.691	0.476	2.088
47	90	1.7	0.494	0.001	−0.004	0.337	9137	1.785	0.513	2.283
48	90	1.8	0.466	0.002	−0.005	0.373	10198	1.874	0.546	2.456
49	90	1.9	0.442	0.002	−0.005	0.405	11259	1.948	0.568	2.603
50	90	2.0	0.42	0.003	−0.005	0.434	12320	2.018	0.589	2.763
51	100	1.1	0.807	−0.008	−0.001	−0.088	3236	1.12	0.163	0.909
52	100	1.2	0.74	−0.007	−0.002	0.005	4764	1.273	0.253	1.403
53	100	1.3	0.683	−0.007	−0.003	0.083	6292	1.412	0.321	1.744
54	100	1.4	0.634	−0.005	−0.004	0.15	7820	1.53	0.37	2.016
55	100	1.5	0.592	−0.003	−0.004	0.207	9348	1.634	0.41	2.285
56	100	1.6	0.555	−0.001	−0.004	0.256	10876	1.739	0.449	2.571
57	100	1.7	0.522	0	−0.004	0.3	12404	1.844	0.487	2.813
58	100	1.8	0.493	0.001	−0.005	0.338	13932	1.944	0.521	3.025
59	100	1.9	0.467	0.002	−0.005	0.372	15460	2.022	0.541	3.207
60	100	2.0	0.444	0.003	−0.005	0.402	16987	2.1	0.562	3.411
61	110	1.1	0.837	−0.009	0	−0.129	3866	1.127	0.14	1.13
62	110	1.2	0.767	−0.007	−0.001	−0.032	6024	1.292	0.233	1.711
63	110	1.3	0.708	−0.007	−0.003	0.05	8181	1.44	0.301	2.1
64	110	1.4	0.658	−0.005	−0.003	0.119	10339	1.56	0.348	2.446
65	110	1.5	0.614	−0.004	−0.004	0.179	12497	1.678	0.39	2.787
66	110	1.6	0.576	−0.002	−0.004	0.23	14655	1.796	0.431	3.137
67	110	1.7	0.542	0	−0.004	0.276	16813	1.914	0.469	3.431
68	110	1.8	0.512	0.002	−0.004	0.315	18970	2.01	0.495	3.655
69	110	1.9	0.485	0.003	−0.004	0.35	21128	2.1	0.517	3.921
70	110	2.0	0.46	0.004	−0.004	0.382	23286	2.201	0.544	4.209
71	120	1.1	0.857	−0.009	0.001	−0.156	4693	1.133	0.125	1.38
72	120	1.2	0.786	−0.005	0	−0.057	7678	1.309	0.218	1.977
73	120	1.3	0.725	−0.004	−0.001	0.027	10663	1.447	0.274	2.504
74	120	1.4	0.673	−0.002	−0.002	0.098	13648	1.6	0.333	3.005
75	120	1.5	0.629	−0.001	−0.003	0.16	16633	1.741	0.382	3.391
76	120	1.6	0.589	0	−0.003	0.213	19618	1.86	0.416	3.74
77	120	1.7	0.555	0.002	−0.003	0.259	22603	1.981	0.449	4.131
78	120	1.8	0.524	0.004	−0.004	0.3	25588	2.094	0.478	4.413
79	120	1.9	0.496	0.005	−0.004	0.336	28573	2.198	0.503	4.757
80	120	2.0	0.471	0.006	−0.004	0.368	31558	2.299	0.527	5.012

Table 3. Simulation parameters. The columns from left to right indicate the following: the RBC cell height H, the reduced temperature difference $\Delta T/\Delta T_{on}$, the NOB-II parameter α, the normalised temperature of the centre plane $\widetilde{T}_c$, the normalised density of the centre plane $\widetilde{\rho}_c$, the normalised density difference $\Delta\widetilde{\rho}$, the Rayleigh number Ra, the Nusselt number Nu, the normalised Nusselt number $\widetilde{Nu}$ and the Reynolds number Re.

No.	g	$\Delta T/T_{cr}$	$\Delta T_{ad}/T_{cr}$	α	Nu	Re	$\widetilde{Nu}$	$\langle\lvert\phi_{conv}\rvert\rangle_{x,y}$	$\langle\lvert\phi_{diff}\rvert\rangle_{x,y}$	$\langle\lvert\phi_{comp}\rvert\rangle_{x,y}$
81	3.0010	0.0966×10^{-5}	0.0105	0.109	2.402	2.389	0.866	5.67×10^{-8}	5.27×10^{-8}	8.85×10^{-9}
82	4.50×10^{-5}	0.0731	0.0158	0.216	2.251	2.394	0.773	4.19×10^{-8}	3.53×10^{-8}	1.34×10^{-8}
83	6.00×10^{-5}	0.0641	0.0210	0.328	2.084	2.400	0.670	3.68×10^{-8}	2.68×10^{-8}	1.79×10^{-8}
84	8.00×10^{-5}	0.0603	0.0280	0.465	1.864	2.435	0.534	3.68×10^{-8}	2.01×10^{-8}	2.42×10^{-8}
85	1.00×10^{-4}	0.0609	0.0350	0.576	1.675	2.401	0.417	3.90×10^{-8}	1.58×10^{-8}	2.99×10^{-8}
86	1.25×10^{-4}	0.0645	0.0438	0.680	1.514	2.395	0.318	4.37×10^{-8}	1.27×10^{-8}	3.72×10^{-8}
87	1.50×10^{-4}	0.0698	0.0526	0.753	1.392	2.385	0.242	4.96×10^{-8}	1.05×10^{-8}	4.45×10^{-8}
88	1.75×10^{-4}	0.0761	0.0613	0.806	1.303	2.398	0.187	5.66×10^{-8}	8.89×10^{-9}	5.23×10^{-8}
89	2.00×10^{-4}	0.0830	0.0701	0.844	1.244	2.434	0.151	6.44×10^{-8}	7.88×10^{-9}	6.08×10^{-8}

Table 4. Simulation parameters for $Ra = 10^4$. The columns from left to right indicate the following: the gravity g, the reduced temperature difference $\Delta T/T_{cr}$, the reduced adiabatic temperature difference $\Delta T_{ad}/T_{cr}$, the NOB-II parameter α, the Nusselt number Nu, the Reynolds number Re, the normalised Nusselt number $\widetilde{Nu}$, the spatial-averaged of the absolute value of convection term $\langle\lvert\phi_{conv}\rvert\rangle_{x,y}$, the spatial-averaged of the absolute value of diffusion term $\langle\lvert\phi_{diff}\rvert\rangle_{x,y}$ and the spatial-averaged of the absolute value of compression term $\langle\lvert\phi_{comp}\rvert\rangle_{x,y}$.

References

Accary, G., Bontoux, P. & Zappoli, B. 2009 Turbulent Rayleigh–Bénard convection in a near-critical fluid by three-dimensional direct numerical simulation. *J. Fluid Mech.* **619**, 127–145.

Accary, G., Raspo, I., Bontoux, P. & Zappoli, B. 2005 Reverse transition to hydrodynamic stability through the Schwarzschild line in a supercritical fluid layer. *Phys. Rev. E* **72** (3), 035301.

Ahlers, G., Araujo, F.F., Funfschilling, D., Grossmann, S. & Lohse, D. 2007 Non-Oberbeck-Boussinesq effects in gaseous Rayleigh-Bénard convection. *Phys. Rev. Lett.* **98** (5), 054501.

Ahlers, G., Brown, E., Araujo, F.F., Funfschilling, D., Grossmann, S. & Lohse, D. 2006 Non-Oberbeck–Boussinesq effects in strongly turbulent Rayleigh–Bénard convection. *J. Fluid Mech.* **569**, 409–445.

Ahlers, G., Calzavarini, E., Araujo, F.F., Funfschilling, D., Grossmann, S., Lohse, D. & Sugiyama, K. 2008 Non-Oberbeck-Boussinesq effects in turbulent thermal convection in ethane close to the critical point. *Phys. Rev. E* **77** (4), 046302.

Amiroudine, S., Bontoux, P., Larroudé, P., Gilly, B. & Zappoli, B. 2001 Direct numerical simulation of instabilities in a two-dimensional near-critical fluid layer heated from below. *J. Fluid Mech.* **442**, 119–140.

Amiroudine, S. & Zappoli, B. 2003 Piston-effect-induced thermal oscillations at the Rayleigh-Bénard threshold in supercritical ^{3}He. *Phys. Rev. Lett.* **90** (10), 105303.

Ashkenazi, S. & Steinberg, V. 1999 High Rayleigh number turbulent convection in a gas near the gas-liquid critical point. *Phys. Rev. Lett.* **83** (18), 3641–3644.

Bouafia, M. & Daube, O. 2021 Rayleigh-Bénard convection in 3he near its critical point. *Intl Commun. Heat Mass Transfer* **120**, 104820.

Carlès, P. & Ugurtas, B. 1999 The onset of free convection near the liquid–vapour critical point Part I: Stationary initial state. *Physica D* **126** (1-2), 69–82.

Carlès, P. & El Khouri, L. 2001 Near-critical fluids as experimental models for geophysical flows: the case of internal gravity waves. *Phys. Fluids* **13** (12), 3775–3782.

Chen, H., Kandasamy, S., Orszag, S., Shock, R., Succi, S. & Yakhot, V. 2003 Extended Boltzmann kinetic equation for turbulent flows. *Science* **301** (5633), 633–636.

Chen, J., Ahmad, S., Deng, W., Cai, J. & Zhao, J. 2022 Micro/nanoscale surface on enhancing the microchannel flow boiling performance: A Lattice Boltzmann simulation. *Appl. Therm. Engng* **205**, 118036.

Chiwata, Y. & Onuki, A. 2001 Thermal plumes and convection in highly compressible fluids. *Phys. Rev. Lett.* **87** (14), 144301.

Clever, R.M. & Busse, F.H. 1974 Transition to time-dependent convection. *J. Fluid Mech.* **65** (4), 625–645.

Demou, A.D. & Grigoriadis, D.G.E. 2019 Direct numerical simulations of Rayleigh–Bénard convection in water with non-Oberbeck–Boussinesq effects. *J. Fluid Mech.* **881**, 1073–1096.

Elliott, J.R. & Lira, C.T. 2012 *Introductory Chemical Engineering Thermodynamics*. Prentice Hall.

FURUKAWA, A. & ONUKI, A. 2002 Convective heat transport in compressible fluids. *Phys. Rev. E* **66** (1), 016302.

GAO, Y., YU, Y., YANG, L., QIN, S. & HOU, G. 2021 Development of a coupled simplified Lattice Boltzmann method for thermal flows. *Comput. Fluids* **229**, 105042.

GITERMAN, M.SH & SHTEINBERG, V.A. 1970 Criteria for commencement of convection in a liquid close to the critical point. *High Temp.* **8** (4), 754.

GONG, S., HU, Z. & CHENG, P. 2024 A mesoscopic approach for nanoscale evaporation heat transfer characteristics. *Intl J. Heat Mass Transfer* **231**, 125856.

GUO, Z., ZHENG, C. & SHI, B. 2002 Discrete lattice effects on the forcing term in the lattice Boltzmann method. *Phys. Rev. E* **65** (4), 046308.

HE, X. & DOOLEN, G.D. 2002 Thermodynamic foundations of kinetic theory and lattice Boltzmann models for multiphase flows. *J. Stat. Phys.* **107** (1/2), 309–328.

HORN, S., SHISHKINA, O. & WAGNER, C. 2013 On non-Oberbeck–Boussinesq effects in three-dimensional Rayleigh–Bénard convection in glycerol. *J. Fluid Mech.* **724**, 175–202.

HUANG, J., ZHOU, Y., HUANG, Y., LUO, Q., YUAN, Y., YANG, C. & HU, W. 2024 Experimental study of pressure drop oscillation in a supercritical carbon dioxide natural circulation loop. *Intl J. Heat Mass Transfer* **220**, 125005.

HUANG, R. & WU, H. 2016 Third-order analysis of pseudopotential lattice Boltzmann model for multiphase flow. *J. Comput. Phys.* **327**, 121–139.

JIANG, M., XU, Z.G. & ZHOU, Z.P. 2021 Pore-scale investigation on reactive flow in porous media considering dissolution and precipitation by LBM. *J. Petrol. Sci. Engng* **204**, 108712.

JOHNSTON, H. & DOERING, C.R. 2009 Comparison of turbulent thermal convection between conditions of constant temperature and constant Flux. *Phys. Rev. Lett.* **102** (6), 064501.

KOGAN, A.B. & MEYER, H. 2001 Heat transfer and convection onset in a compressible fluid: ^{3}He near the critical point. *Phys. Rev. E* **63** (5), 056310.

KOGAN, A.B., MURPHY, D. & MEYER, H. 1999 Rayleigh-Bénard convection onset in a compressible fluid: ^{3}He near T_C. *Phys. Rev. Lett.* **82** (23), 4635–4638.

LI, Q., KANG, Q.J., FRANCOIS, M.M., HE, Y.L. & LUO, K.H. 2015 Lattice Boltzmann modeling of boiling heat transfer: The boiling curve and the effects of wettability. *Intl J. Heat Mass Transfer* **85**, 787–796.

LOHSE, DETLEF & SHISHKINA, OLGA 2024 Ultimate Rayleigh-Bénard turbulence. *Rev. Mod. Phys.* **96** (3), 035001.

LOHSE, D. & XIA, K.-Q. 2010 Small-scale properties of turbulent Rayleigh-Bénard convection. *Annu. Rev. Fluid Mech.* **42** (2010), 335–364.

MEYER, H. & KOGAN, A.B. 2002 Onset of convection in a very compressible fluid: the transient toward steady state. *Phys. Rev. E* **66** (5), 056310.

MISALE, M., GARIBALDI, P., PASSOS, J.C. & DE BITENCOURT, G.G. 2007 Experiments in a single-phase natural circulation mini-loop. *Exp. Therm. Fluid Sci.* **31** (8), 1111–1120.

MOUKALLED, F., MANGANI, L. & DARWISH, M. 2016 *The Finite Volume Method in Computational Fluid Dynamics: An Advanced Introduction with OpenFOAM® and Matlab*. Spinger.

PAN, X. & CHOI, J.-IL 2023 Non-Oberbeck–Boussinesq effects in two-dimensional Rayleigh–Bénard convection of different fluids. *Phys. Fluids* **35** (9), 095108.

PAN, X. & CHOI, J.-IL 2024 Effects of inclination angle on Rayleigh–Bénard convection under non-Oberbeck–Boussinesq approximation in air. *Intl Commun. Heat Mass Transfer* **151**, 107255.

PANDEY, A., SCHUMACHER, J. & SREENIVASAN, K.R. 2021 Non-Boussinesq convection at low Prandtl numbers relevant to the Sun. *Phys. Rev. Fluids* **6** (10), 100503.

PENG, D.-Y. & ROBINSON, D.B. 1976 A new two-constant equation of state. *Ind. Engng Chem. Fundamen.* **15** (1), 59–64.

QIAN, Y.-H., D'HUMIÈRES, D. & LALLEMAND, P. 1992 Lattice BGK Models for Navier-Stokes Equation. *Europhys. Lett.* **17** (6), 479–484.

SHAH, S.W.A., JIANG, X., LI, Y., CHEN, G., LIU, J., GAO, Y., AHMAD, S., ZHAO, J. & PAN, C. 2023 Flow boiling in a counter flow straight microchannel pair: LBM study. *Intl Commun. Heat Mass Transfer* **147**, 106990.

SHAN, X. 1997 Simulation of Rayleigh-Bénard convection using a lattice Boltzmann method. *Phys. Rev. E* **55** (3), 2780–2788.

SHAN, X. & CHEN, H. 1993 Lattice Boltzmann model for simulating flows with multiple phases and components. *Phys. Rev. E* **47** (3), 1815–1819.

SHAN, X. & CHEN, H. 1994 Simulation of nonideal gases and liquid-gas phase transitions by the lattice Boltzmann equation. *Phys. Rev. E* **49** (4), 2941–2948.

SHEN, B. & ZHANG, P. 2012 Rayleigh–Bénard convection in a supercritical fluid along its critical isochore in a shallow cavity. *Intl J. Heat Mass Transfer* **55** (23), 7151–7165.
SHISHKINA, O. & WAGNER, S. 2016 Prandtl-number dependence of heat transport in Laminar horizontal convection. *Phys. Rev. Lett.* **116** (2), 024302.
SHISHKINA, O., WEISS, S. & BODENSCHATZ, E. 2016 Conductive heat flux in measurements of the Nusselt number in turbulent Rayleigh-Bénard convection. *Phys. Rev. Fluids* **1** (6), 062301.
SUGIYAMA, K., CALZAVARINI, E., GROSSMANN, S. & LOHSE, D. 2009 Flow organization in two-dimensional non-Oberbeck–Boussinesq Rayleigh–Bénard convection in water. *J. Fluid Mech.* **637**, 105–135.
TONG, Z., CHEN, Y. & MALKAWI, A. 2017 Estimating natural ventilation potential for high-rise buildings considering boundary layer meteorology. *Appl. Energy* **193**, 276–286.
TOPPALADODDI, S. & WETTLAUFER, J.S. 2018 Penetrative convection at high Rayleigh numbers. *Phys. Rev. Fluids* **3** (4), 043501.
VALORI, V., ELSINGA, G., ROHDE, M., TUMMERS, M., WESTERWEEL, J. & VAN DER, H. 2017 Experimental velocity study of non-Boussinesq Rayleigh-Bénard convection. *Phys. Rev. E* **95** (5), 053113.
WAN, Z.-H., WANG, Q., WANG, B., XIA, S.N., ZHOU, Q. & SUN, D.-J. 2020 On non-Oberbeck–Boussinesq effects in Rayleigh–Bénard convection of air for large temperature differences. *J. Fluid Mech.* **889**, A10.
WANG, Q., ZHOU, Q., WAN, Z.-H. & SUN, D.-J. 2019 Penetrative turbulent Rayleigh013; Bénard convection in two and three dimensions. *J. Fluid Mech.* **870**, 718–734.
WINCHESTER, P., HOWELL, P.D. & DALLAS, V. 2022 The onset of zonal modes in two-dimensional Rayleigh–Bénard convection. *J. Fluid Mech.* **939**, A8.
WU, X.-Z. & LIBCHABER, A. 1991 Non-Boussinesq effects in free thermal convection. *Phys. Rev. A* **43** (6), 2833–2839.
YIK, H., VALORI, V. & WEISS, S. 2020 Turbulent Rayleigh-Bénard convection under strong non-Oberbeck-Boussinesq conditions. *Phys. Rev. Fluids* **5** (10), 103502.
YU, J., GOLDFADEN, A., FLAGSTAD, M. & SCHEEL, J.D. 2017 Onset of Rayleigh-Bénard convection for intermediate aspect ratio cylindrical containers. *Phys. Fluids* **29** (2), 024107.
ZAPPOLI, B., BAILLY, D., GARRABOS, Y., LE NEINDRE, B., GUENOUN, P. & BEYSENS, D. 1990 Anomalous heat transport by the piston effect in supercritical fluids under zero gravity. *Phys. Rev. A* **41** (4), 2264–2267.
ZHANG, J., CHILDRESS, S. & LIBCHABER, A. 1997 Non-Boussinesq effect: thermal convection with broken symmetry. *Phys. Fluids* **9** (4), 1034–1042.
ZOU, Q. & HE, X. 1997 On pressure and velocity boundary conditions for the Lattice Boltzmann BGK model. *Phys. Fluids* **9** (6), 1591–1598.